The Astrophysical Journal, 977:250 (21pp), 2024 December 20 https://doi.org/10.3847/1538-4357/ad9027

UNCOVER: A NIRSpec Census of Lensed Galaxies at $z = 8.50$–13.08 Probing a High-AGN Fraction and Ionized Bubbles in the Shadow

Seiji Fujimoto[1,31], Bingjie Wang[2,3,4], John R. Weaver[5], Vasily Kokorev[6], Hakim Atek[7], Rachel Bezanson[8], Ivo Labbe[9], Gabriel Brammer[10], Jenny E. Greene[11], Iryna Chemerynska[7], Pratika Dayal[6], Anna de Graaff[12], Lukas J. Furtak[13], Pascal A. Oesch[10,14], David J. Setton[8], Sedona H. Price[8], Tim B. Miller[15,16], Christina C. Williams[17,18], Katherine E. Whitaker[5], Adi Zitrin[13], Sam E. Cutler[5], Joel Leja[2,3,4], Richard Pan[19], Dan Coe[20,21,22], Pieter van Dokkum[15], Robert Feldmann[23], Yoshinobu Fudamoto[24,25], Andy D. Goulding[11], Gourav Khullar[8], Danilo Marchesini[19], Michael Maseda[26], Themiya Nanayakkara[9], Erica J. Nelson[27], Renske Smit[28], Mauro Stefanon[29,30], and Andrea Weibel[14]

[1] Department of Astronomy, The University of Texas at Austin, Austin, TX 78712, USA; fujimoto@utexas.edu
[2] Department of Astronomy & Astrophysics, The Pennsylvania State University, University Park, PA 16802, USA
[3] Institute for Computational & Data Sciences, The Pennsylvania State University, University Park, PA 16802, USA
[4] Institute for Gravitation and the Cosmos, The Pennsylvania State University, University Park, PA 16802, USA
[5] Department of Astronomy, University of Massachusetts, Amherst, MA 01003, USA
[6] Kapteyn Astronomical Institute, University of Groningen, 9700 AV Groningen, The Netherlands
[7] Institut d'Astrophysique de Paris, CNRS, Sorbonne Université, 98bis Boulevard Arago, 75014 Paris, France
[8] Department of Physics and Astronomy and PITT PACC, University of Pittsburgh, Pittsburgh, PA 15260, USA
[9] Centre for Astrophysics and Supercomputing, Swinburne University of Technology, Melbourne, VIC 3122, Australia
[10] Cosmic Dawn Center (DAWN), Niels Bohr Institute, University of Copenhagen, Jagtvej 128, København N, DK-2200, Denmark
[11] Department of Astrophysical Sciences, Princeton University, 4 Ivy Lane, Princeton, NJ 08544, USA
[12] Max-Planck-Institut für Astronomie, Königstuhl 17, D-69117 Heidelberg, Germany
[13] Physics Department, Ben-Gurion University of the Negev, P.O. Box 653, Be'er-Sheva 84105, Israel
[14] Department of Astronomy, University of Geneva, Chemin Pegasi 51, 1290 Versoix, Switzerland
[15] Department of Astronomy, Yale University, New Haven, CT 06511, USA
[16] Center for Interdisciplinary Exploration and Research in Astrophysics (CIERA) and Department of Physics and Astronomy, Northwestern University, 1800 Sherman Ave, Evanston, IL 60201, USA
[17] NSFs National Optical-Infrared Astronomy Research Laboratory, 950 N. Cherry Avenue, Tucson, AZ 85719, USA
[18] Steward Observatory, University of Arizona, 933 N. Cherry Avenue, Tucson, AZ 85721, USA
[19] Department of Physics and Astronomy, Tufts University, 574 Boston Avenue, Medford, MA 02155, USA
[20] Space Telescope Science Institute, 3700 San Martin Drive, Baltimore, MD 21218, USA
[21] Association of Universities for Research in Astronomy (AURA), Inc. for the European Space Agency (ESA), 1331 Pennsylvania Ave. NW, Washington, DC 20004, USA
[22] Center for Astrophysical Sciences, Department of Physics and Astronomy, The Johns Hopkins University, 3400 N. Charles Street, Baltimore, MD 21218, USA
[23] Institute for Computational Science, University of Zurich, Zurich CH-8057, Switzerland
[24] Waseda Research Institute for Science and Engineering, Faculty of Science and Engineering, Waseda University, 3-4-1 Okubo, Shinjuku, Tokyo 169-8555, Japan
[25] National Astronomical Observatory of Japan, 2-21-1 Osawa, Mitaka, Tokyo, Japan
[26] Department of Astronomy, University of Wisconsin-Madison, 475 N. Charter Street, Madison, WI 53706, USA
[27] Department for Astrophysical and Planetary Science, University of Colorado, Boulder, CO 80309, USA
[28] Astrophysics Research Institute, Liverpool John Moores University, 146 Brownlow Hill, Liverpool L3 5RF, UK
[29] Departament d'Astronomia i Astrofísica, Universitat de València, C. Dr. Moliner 50, E-46100 Burjassot, València, Spain
[30] Unidad Asociada CSIC "Grupo de Astrofísica Extragaláctica y Cosmología," Instituto de Física de Cantabria, Universitat de València, València, Spain
Received 2023 August 25; revised 2024 November 3; accepted 2024 November 5; published 2024 December 18

Abstract

We present JWST NIRSpec prism spectroscopy of lensed galaxies at $z \gtrsim 9$ found behind the massive galaxy cluster Abell 2744 in the UNCOVER Cycle 1 Treasury Program. We confirm the redshift via emission lines and/or the Lyα break for 10 galaxies at $z = 8.50$–13.08 down to $M_V = -17.3$. We achieve a 100% confirmation rate for $z > 9$ candidates reported in H. Atek et al. Using six sources with multiple line detections, we find that offsets in redshift estimates between the lines and the Lyα break alone can be ± 0.2, raising caution in designing future follow-up spectroscopy for the break-only sources with the Atacama Large Millimeter/submillimeter Array. With spec-z-confirmed sources in UNCOVER and the literature, we derive lower limits on the rest-frame ultraviolet (UV) luminosity function (LF) at $z \simeq 9$–12 and find that these lower limits agree with recent photometric measurements. We identify at least two unambiguous and several possible active galactic nucleus (AGN) systems based on X-ray, broad Hβ, high ionization lines, and excess in the UV LF. This requires the AGN LFs at $z \simeq 9$–10 to be comparable or even higher than the X-ray AGN LF estimated at $z \sim 6$ and suggests a plausible cause of the high abundance of $z > 9$ galaxies claimed in the recent photometric measurements is AGNs. One UV-luminous source is confirmed at the same redshift as a broad-line AGN at $z = 8.50$ with a physical separation of 380 kpc in the source plane. These

[31] Hubble Fellow.

two sources show emission blueward of Lyα, indicating a giant ionized bubble enclosing them with a radius of 7.69 ± 0.18 pMpc. Our results imply that AGNs have a nonnegligible contribution to cosmic reionization.

Unified Astronomy Thesaurus concepts: High-redshift galaxies (734); Early universe (435); Luminosity function (942); Reionization (1383); Active galactic nuclei (16)

1. Introduction

Studying early galaxies provides key clues to understanding fundamental cosmological questions such as dark matter assembly, the development of large-scale structure, the emergence of the first galaxies and black holes, and the processes that govern cosmic reionization and early galaxy formation and evolution (e.g., P. Dayal & A. Ferrara 2018; K. Inayoshi et al. 2020). In the last decades, deep Hubble Space Telescope (HST) surveys have succeeded in discovering thousands of galaxies in the Epoch of Reionization (EOR) $6 \lesssim z \lesssim 11$, providing valuable photometric insights for these galaxies, including an initial characterization of the stellar component, in terms of unobscured star formation rates (SFRs) and sizes (e.g., R. S. Ellis et al. 2013; R. J. Bouwens et al. 2015; S. L. Finkelstein et al. 2015; P. A. Oesch et al. 2016; R. Bhatawdekar et al. 2019).

The advent of JWST (J. P. Gardner et al. 2023) has led to significant progress in discovering and investigating galaxies at very early cosmic epochs. As demonstrated in the Early Release Observations (K. Pontoppidan et al. 2022) and the Early Release Science (ERS) programs (e.g., T. Treu et al. 2022; S. L. Finkelstein et al. 2023), dozens of high-redshift galaxy candidates have been identified at $z \simeq 9$–17 toward both lensing clusters and blank fields (e.g., H. Atek et al. 2023a, 2023b; M. Castellano et al. 2022; S. L. Finkelstein et al. 2022b, 2023; R. P. Naidu et al. 2022b; N. J. Adams et al. 2023; D. Austin et al. 2023; R. J. Bouwens et al. 2023b; L. D. Bradley et al. 2023; C. T. Donnan et al. 2023; Y. Harikane et al. 2023a; I. Labbe et al. 2023a; G. C. K. Leung et al. 2023; T. Morishita & M. Stiavelli 2023; C. C. Williams et al. 2023; H. Yan et al. 2023). Their abundance at the bright end ($M_{\rm UV} \lesssim -20$) exceeds nearly all theoretical predictions so far (e.g., P. S. Behroozi & J. Silk 2015; P. Dayal et al. 2017; L. Y. A. Yung et al. 2019, 2020; P. Behroozi et al. 2019, 2020; R. Dave et al. 2019; S. M. Wilkins et al. 2022, 2023; R. Kannan et al. 2023; C. A. Mason et al. 2023; V. Mauerhofer & P. Dayal 2023), suggesting several possibilities, including that star formation in early systems is dominated by a top-heavy initial mass function (IMF), complete lack of dust attenuation, stochastic star formation, and/or the emergence of the active galactic nucleus (AGN) population (e.g., N. Menci et al. 2022; F. Pacucci et al. 2022; M. Boylan-Kolchin 2023; A. Ferrara et al. 2023; S. L. Finkelstein et al. 2023; Y. Harikane et al. 2023a; C. C. Lovell et al. 2023; G. Sun et al. 2023).

JWST NIRSpec follow-up spectroscopy has been performed for several bright galaxy candidates at $z \simeq 10$–17, including Director's Discretionary Time (DDT) programs. These follow-up observations confirm the source redshifts via emission lines and/or the unambiguous Lyα break feature at $z = 9.5$–13.2 (P. Arrabal Haro et al. 2023a, 2023b; A. J. Bunker et al. 2023; E. Curtis-Lake et al. 2023; G. Roberts-Borsani et al. 2023; B. Wang et al. 2023a; H. Williams et al. 2023; Y. Harikane et al. 2024; T. Y.-Y. Hsiao et al. 2024). However, one remarkably UV-bright ($M_{\rm UV} \simeq$ –22) galaxy candidate at $z \simeq 16$ turns out to be at $z = 4.9$ with strong emission lines and red continuum that mimic the expected colors of more distant objects (R. P. Naidu et al. 2022a; P. Arrabal Haro et al. 2023a; S. Fujimoto et al. 2023b; J. McKinney et al. 2023; J. A. Zavala et al. 2023). Recent JWST spectroscopic observations also find a numerous number of faint AGN populations at $z \simeq 4$–7 (e.g., Y. Harikane et al. 2023b; D. D. Kocevski et al. 2023; R. Maiolino et al. 2024a; J. Matthee et al. 2024), indicative of steeper faint ends in the quasar/AGN luminosity functions (LFs) than suggested in previous studies, and some studies suggest the identification of AGNs even at higher redshifts at $z \sim 9$–11 (A. D. Goulding et al. 2023; R. L. Larson et al. 2023; R. Maiolino et al. 2024b). These results indicate the critical importance of spectroscopy in order to foremost confirm the high-redshift nature of galaxy candidates and consequently verify earlier (photometric) claims of a high abundance of $z \gtrsim 9$ galaxy candidates in order to investigate its origins.

In this paper, we present JWST NIRSpec prism follow-up observations of $z \gtrsim 9$ galaxy candidates, including an X-ray-luminous supermassive black hole (A. D. Goulding et al. 2023) and two $z > 12$ galaxies (B. Wang et al. 2023a), all identified in the Cycle 1 Treasury program of Ultradeep NIRSpec and NIRCam Observations before the EOR (UNCOVER) survey (#2561; PIs: I. Labbe and R. Bezanson; R. Bezanson et al. 2024). This is the most extensive follow-up program with NIRSpec prism in Cycle 1 for JWST-selected galaxy candidates toward a massive lensing cluster, providing a unique opportunity for a spectroscopic study for a large sample in the early Universe over a wide UV luminosity range. Following the recent successful spectroscopic confirmation of the high-redshift galaxies with JWST, this enlarges the spectroscopic sample at $z \gtrsim 9$ for faint sources ($M_{\rm UV} > -19$) by a factor of $\sim$3 and further allows detailed investigations into the UV LF shape and the characterization of the high-redshift galaxy population newly identified with JWST. In Section 2, we briefly describe observations and data processing. Section 3 outlines our methods and results for the redshift measurements. In Section 4, we present our UV LF measurements at $z \simeq 9$–12 and a potential high abundance of AGNs. In Section 5, we report a discovery of a giant ionized bubble at $z = 8.5$ and discuss the contribution of AGNs to forming it. We summarize this study in Section 6. Throughout this paper, we assume a flat Universe with $\Omega_{\rm m} = 0.3$, $\Omega_\Lambda = 0.7$, $\sigma_8 = 0.8$, and $H_0 = 70$ km s^{-1} Mpc^{-1} (G. Hinshaw et al. 2013). All magnitudes are expressed in the AB system (J. B. Oke & J. E. Gunn 1983). The significance of X-ray detection in UHZ1 (A. D. Goulding et al. 2023) increases from follow-up Chandra observations (A. Bogdan et al. 2024, in preparation), and we regard UHZ1 as an X-ray AGN throughout the paper.

2. Observations and Data Processing

The JWST/NIRCam (M. J. Rieke et al. 2003, 2005; C. A. Beichman et al. 2012; M. J. Rieke et al. 2023) and NIRSpec (P. Jakobsen et al. 2022) data employed in this paper were taken as a part of the UNCOVER survey (R. Bezanson et al. 2024). While the complete descriptions of the NIRCam observations and NIRSpec observations are presented in J. R. Weaver et al. (2024) and S. H. Price et al. (2024),

respectively, we briefly describe the reduction employed in this paper in the following subsection.

2.1. UNCOVER Survey

Abell 2744 (A2744) is among the most extensively studied massive galaxy clusters at $z = 0.308$ and serves as the focal point of the UNCOVER survey. A2744 has been subjected to detailed observations using the HST as one of the clusters observed in the Hubble Frontier Field (HFF) survey (J. M. Lotz et al. 2017). The sky area of A2744 has a low infrared background, and its high magnification areas match well with the NIRCam field of view (FOV). Multiple JWST Cycle 1 and 2 observations, including Guaranteed Time Observations, ERS, General Observers (GO), and DDT programs, have been conducted and further planned toward this cluster. Specifically, a GO treasury program under the JWST Cycle 1—UNCOVER (#2561; PIs I. Labbe and R. Bezanson)—is designed to acquire in-depth NIRCam and NIRSpec observations over an extended $4' \times 6'$ area (R. Bezanson et al. 2024), enveloping the area with magnifications of $\mu \geqslant 2$ encompassing the primary cluster observed in HFF and two supplementary cluster cores in the northern and northwest regions (L. J. Furtak et al. 2023b). UNCOVER consists of two parts: (1) a deep NIRCam preimaging mosaic in seven filters for ∼4–6 hr per band taken in 2022 November, and (2) an ∼24 hr NIRSpec prism low-resolution follow-up of NIRCam-detected high-redshift galaxies in 2023 July–August.

2.2. NIRCam Data and Target Selection

The galaxies discussed in this paper are selected from the UNCOVER NIRCam data taken in 2022 November (R. Bezanson et al. 2024). The J. R. Weaver et al. (2024) photometric catalog includes the measurements over the full NIRCam wavelength range in the F115W, F150W, F200W, F277W, F356W, F410M, and F444W filters, which have exposures of 3.7–6.0 hr per filter, as well as existing HST Advanced Camera for Surveys and WFC3 F606W, F814W, F105W, F125W, F140W, and F160W filters. The galaxy candidates at $z \gtrsim 9$ are selected based on photometric redshift $z_{\rm photo}$ estimates from several spectral energy distribution (SED) analyses led by UNCOVER team members (e.g., H. Atek et al. 2023b; B. Wang et al. 2024), while we also add several sources by visually checking the NIRCam SEDs and image cutouts in a less conservative sample selected based on photometric redshifts inferred from `EAZY` (G. B. Brammer et al. 2008) and `Prospector` (B. D. Johnson et al. 2021; B. Wang et al. 2023b) in order not to miss possible candidates. Together with other exciting high-redshift source candidates (e.g., faint AGNs, quiescent galaxies, and strongly magnified and multiply imaged sources), the NIRSpec Multiobject Spectroscopy (MOS) configurations with the multishutter array (MSA) were designed to maximize the number of observed exciting candidates. We used seven MSA masks in our observations, referred to as MSA-1 through MSA-7. In this paper, we present 10 sources whose redshifts are successfully confirmed at $z \geqslant 8.5$ among a total of 680 MOS targets (Section 3.1). In Figure 1, we show the distribution of the 10 galaxies in A2744, and Figure 2 presents their NIRCam red, green, and blue (RGB) color images with their MSA configurations.

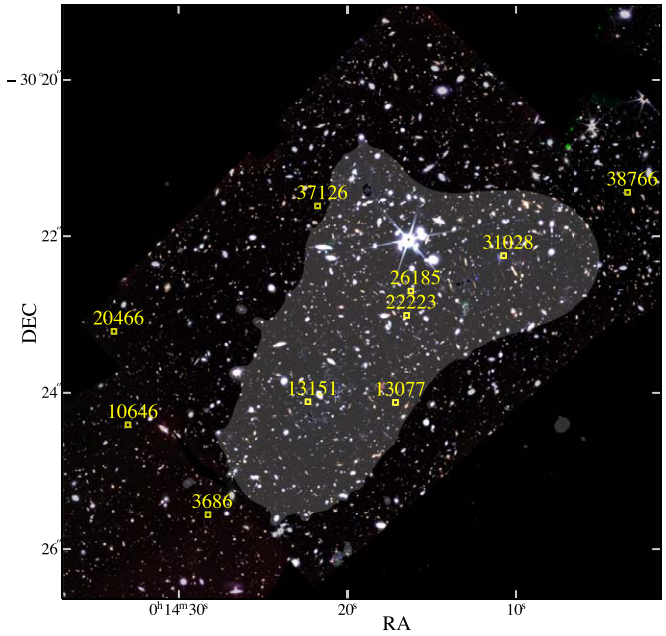

Figure 1. NIRCam RGB (R: F444W, G: F356W, and B: F277W) map of A2744 taken in UNCOVER (R. Bezanson et al. 2024). The white-shaded region indicates the highly magnified area with magnifications of $\geqslant 2$ (L. J. Furtak et al. 2023b). The yellow squares show the positions of the 10 sources that are spectroscopically confirmed at $z \geqslant 8.5$ in UNCOVER.

2.3. NIRSpec Data Processing

The data were reduced using the STScI JWST pipeline for Level 1 data products and processed with `msaexp` v0.6.10,[32] which is built on custom routines for further corrections in addition to the STScI pipeline routines to generate Level 2 and 3 products. The full descriptions of the NIRSpec data reduction will be presented in S. H. Price et al. (2024; see also A. D. Goulding et al. 2023; B. Wang et al. 2023a). Briefly, the data reduction was processed from the raw data files by using the `Detector1Pipeline` routine in combination with the latest batch of reference files (`jwst_1100.pmap`) to correct detector-level artifacts and to convert the data into count rate images. We then leverage custom preprocessing procedures from `msaexp` to correct for $1/f$ noise, remove "snowballs" and bias on a per exposure basis before executing several STScI routines from the `Spec2Pipeline` to generate the final 2D cutout images. The `AssignWcs`, `Extract2dStep`, `FlatFieldStep`, and `PhotomStep` routines are utilized to perform world coordinate system registration, flat-fielding, and flux calibration. The `PathLossStep` accounting for the slit-loss correction is turned off at this stage of the reduction process. Instead, we perform slit-loss corrections by fitting for a polynomial calibration vector of order two (after applying a wavelength-independent calibration to scale the normalization of the spectrum to the photometry). We undertake background subtraction locally, employing a three-shutter nod pattern before mapping the resultant images onto a uniform grid. From that point, we extract the spectra optimally through an inverse-variance weighted kernel derived by collapsing the 2D spectrum along the dispersion axis and fitting the ensuing signal along the spatial axis with a Gaussian profile. In some cases (ID31028, ID13151, and ID13077), this Gaussian fitting is challenging due to the low signal-to-noise ratio (SNR) of the

[32] https://github.com/gbrammer/msaexp

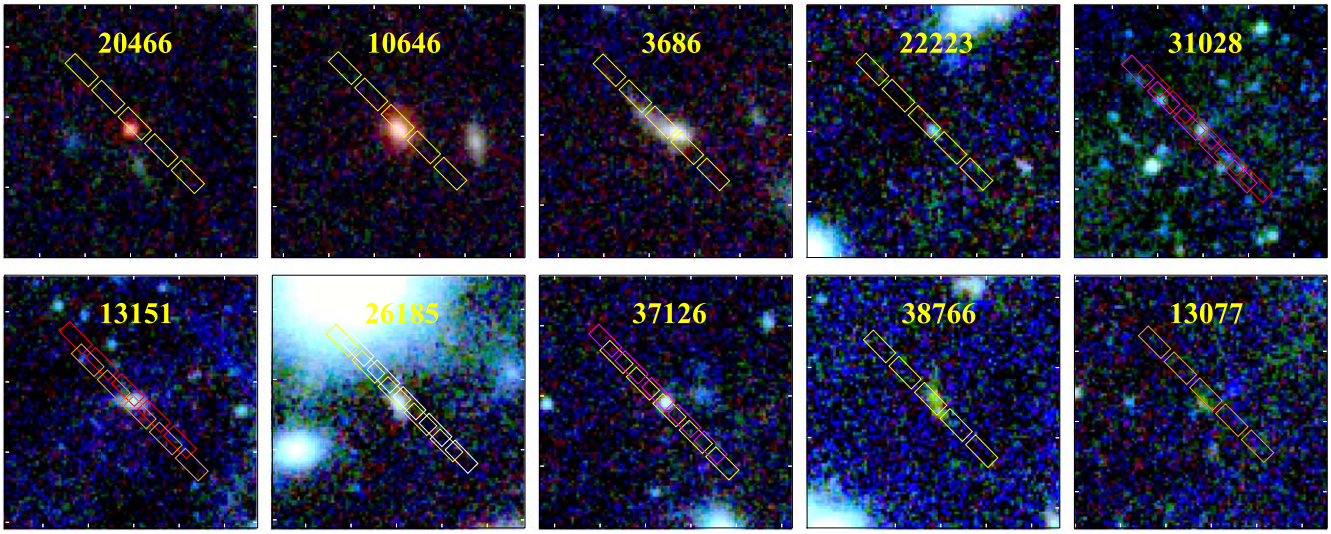

Figure 2. Zoom-in $3\farcs6 \times 3\farcs6$ NIRCam RGB (R: F444W, G: F356W, and B: F277W) cutouts of the 10 sources whose spec-z are successfully confirmed. The rectangles show the shutter configurations, where the standard three-shutter slitlets and a three-point nodding were adopted, and thus the five shutter positions are presented. The white, magenta, yellow, orange, red, and cyan rectangles represent our MSA observations of MSA-2, 3, 4, 5, 6, and 7, respectively, where MSA-5, 6, and 7 overlap nearly entirely.

trace or the contamination of nearby sources in the shutters, and we manually set the Gaussian profile for the extraction. In Figure 3, we show the 2σ range of the Gaussian profile used to extract the 2D spectrum.

3. Spectroscopic Redshift

3.1. Measurements and Results

We perform a template fitting to the NIRSpec prism 1D spectra to measure the source redshift using `eazy` (G. B. Brammer et al. 2008) implemented in `msaexp`. The `eazy` code adopts a set of templates added in a nonnegative linear combination, allowing us to securely measure the source redshift via any faint emission lines as well as the Lyα break feature at $z \gtrsim 10$. We use the `corr_sfhz_13` subset models,[33] which include redshift-dependent star formation history and dust attenuation. We additionally include the best-fit SED template of the JWST-observed extreme objects of the strong-emission-line galaxy at $z = 8.5$ (ID4590) from A. C. Carnall et al. (2023) and an obscured AGN at $z = 4.50$ in the MACJ0647 lensing cluster (M. Killi et al. 2024) to adequately model the potential strong emission lines and obscured AGNs that have been frequently reported in recent NIRSpec studies (e.g., Y. Harikane et al. 2023b; D. D. Kocevski et al. 2023; L. J. Furtak et al. 2024). We include the absorption of the intergalactic medium (IGM) in the fitting to include the damping Lyα wing effect, especially toward high redshifts (e.g., E. Curtis-Lake et al. 2023; K. E. Heintz et al. 2024; H. Umeda et al. 2024). We search for the best solution from χ^2 minimization over the redshift range of $z = 0.1$–20 for all the MOS targets. Fixing the best-fit redshift estimate, we also conduct a spline fitting with `msaexp` to the continuum combined with the single Gaussian for each emission line to evaluate the significance level for each faint emission line at the corresponding wavelength.

Figure 3 summarizes the 2D and 1D spectra and the likelihood of the redshift $P(z)$ for 10 sources whose redshifts are estimated at $z \geqslant 8.5$ in our analysis. All these 10 sources show that the likelihood of z below $z = 8.0$ $P(z < 8)$ is $\ll 3 \times 10^{-7}$. This suggests the significance of our spectroscopic redshift confirmation being well beyond the 5σ level, and we regard these 10 sources as the successful spec-z-confirmed sources in this paper. In Figure 3, we also present vertical lines highlighting the wavelengths of the Lyα break and any faint emission lines detected with a SNR $\geqslant 2.5$ via the spline + Gaussian fit to the prism spectrum with the source redshift fixed at the one obtained from the template fitting. From seven out of 10 sources, we detect faint emission lines at secure SNRs ($\geqslant 5$), while the redshift is also constrained for the other three sources via the Lyα break feature.

Among these 10 prism spectra, we detect an unambiguous broad-line (BL) Hβ component in ID20466 spectroscopically confirmed at $z = 8.50$. The line width of the BL Hβ is estimated to be FWHM $= 3439 \pm 413$ km s^{-1}. The Balmer decrement measurement via Hγ/Hβ suggests a heavily dust-obscured nature of $A_V = 2.1^{+1.1}_{-1.0}$ with the Small Magellanic Cloud dust attenuation law. Moreover, it shows a remarkably bright [O III] λ4363 line, resulting in the dust-corrected [O III] λ4363/[O III] λ5008 ratio being 0.32. Such a high ratio cannot be reproduced by typical electron temperatures and electron densities (e.g., D. C. Nicholls et al. 2020), while the high ratio is generally observed in local Seyfert galaxies (e.g., D. E. Osterbrock 1978; M. A. Dopita & R. S. Sutherland 1995; T. Nagao et al. 2001; A. Baskin & A. Laor 2005). From the BL line detection and the extremely high-ionization state, we conclude that ID20466 is the AGN, and we refer the reader to the separate paper of V. Kokorev et al. (2023) for more characterizations and discussions of this source.

Interestingly, we detect uniquely high-ionization emission lines from several other sources. For example, ID10646 shows a remarkable number of emission lines with secure SNRs, including C IV λ1549 and He II λ1640, similar to the AGN candidate of GNz11 (R. Maiolino et al. 2024a). A detailed UV–optical line study (H. Treiber et al. 2024, in preparation) suggests that ID10646 falls on the AGN regime in the equivalent width (EW)–line relation among the C III]

[33] https://github.com/gbrammer/eazy-photoz/tree/master/templates/sfhz

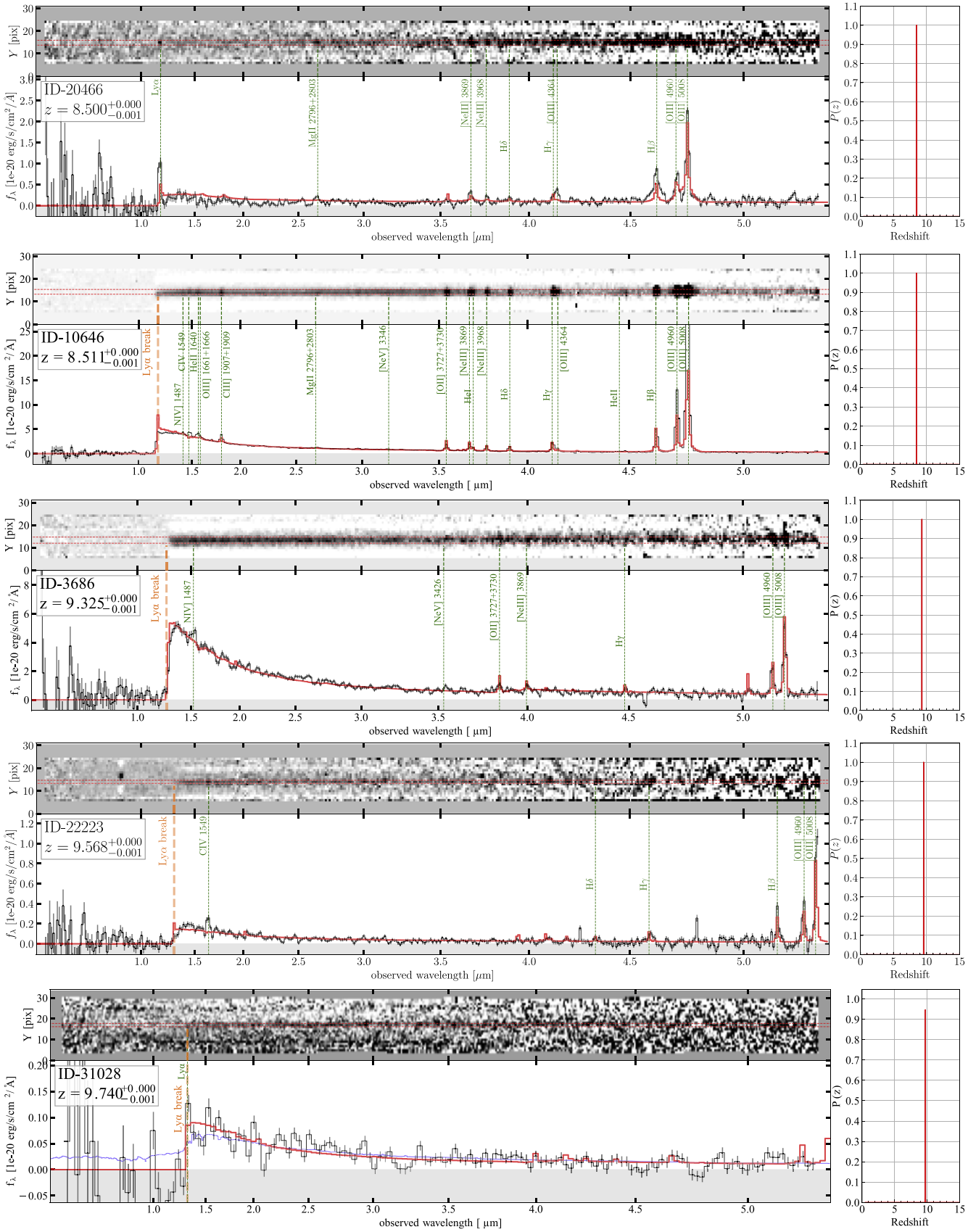

Figure 3. 2D and 1D prism spectra for the 10 sources whose spec-z are successfully confirmed at $z \geqslant 8.5$ in this study. The red horizontal lines indicate the 2σ range of the Gaussian, which is used for extracting the 1D spectrum shown in the bottom panel. The orange and green vertical lines denote wavelengths of the Lyα break and the faint emission lines detected at SNR $\geqslant 2.5$, respectively. The right panel shows the likelihood of the source redshift $P(z)$ estimated from the `eazy` template fitting to the prism spectrum, and the best-fit SED (forced at $z < 6$) is presented with the red (blue) curve overlaid on the 1D spectrum.

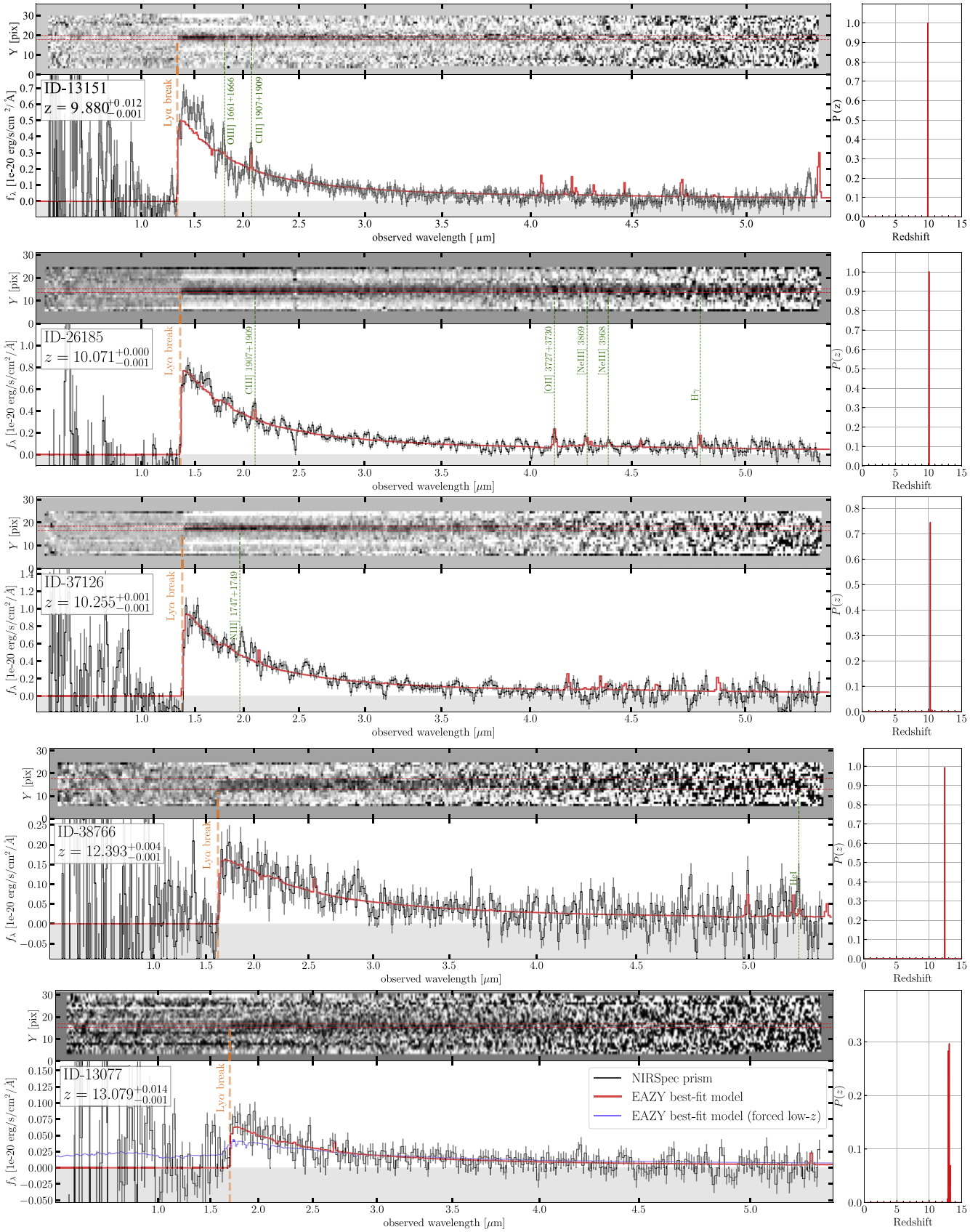

Figure 3. (Continued.)

$\lambda\lambda$1907, 1909, C IV λ1549, and He II λ1640 lines, based on the rest-frame UV–optical line diagnostic for star-forming activity and AGNs (e.g., A. Feltre et al. 2016; M. Hirschmann et al. 2019). This indicates that ID10646 is a plausible AGN candidate. ID3686 also shows a unique excitation feature. The ratio of [O III] λ5008/Hβ is observed to be $16.3^{+21.8}_{-5.9}$, which exceeds the maximum value of $\sim$10 observed in recent NIRSpec studies for galaxies at $z\sim$2–9 and falls in the AGN regime in the [N II], [S II], and [O I] Baldwin–Phillips–Terlevich (BPT) diagrams (e.g., R. L. Sanders et al. 2023). ID3686 falls in the AGN regime also in the mass–excitation diagnostic (e.g., S. Juneau et al. 2014) with a stellar mass estimate of $\sim10^9$ $M_\odot$ for this object (K. Boyett et al. 2024). Given the potential self-subtraction due to its extended morphology and the three-shutter nod method (see Figure 2), we also perform a global background subtraction by using a nearby empty shutter and confirm a similarly high ratio of $11.2^{+4.2}_{-2.4}$ in the central shutter. While the high [O III] λ5008/Hβ ratio is also induced by shock excitation (e.g., L. J. Kewley et al. 2013; M. Hirschmann et al. 2023), we also confirm a high ratio reaching out to $17.5^{+17.5}_{-5.8}$ in the spectrum of the southeast shutter with the global subtraction method, where the emission is more dominated by the compact component in the NIRCam map. These results may also suggest that the uniquely high [O III] λ5008/Hβ ratio in ID3686 is the strong radiation from an AGN. Note that both ID10646 and ID3686 are spatially resolved in the NIRCam filters. However, BL AGNs have also been identified in spatially resolved sources at $z\simeq$4–7 (e.g., Y. Harikane et al. 2023b), and the presence of an AGN does not always require a point-source morphology, depending on the contrast between the host galaxy and AGN. Although a top-heavy IMF in high-z galaxies is also an interesting and plausible possibility to explain the unique excitation features, the top-heavy IMF itself also still needs confirmation from observations. In short, although the origins of the unique excitation features observed in ID10646 and ID3686 are not conclusive for now, AGNs naturally fit with those unique excitation features, and we regard those two sources as potential AGN candidates in the following sections.

In Table 1, we summarize our spectroscopic redshift estimates $z_{\rm spec}$ for our 10 spec-z-confirmed sources, together with basic source properties and the implications of the AGN. We further discuss the potential AGN interpretation of ID10646 and ID3686 in Section 4. In Figure 4, we summarize $M_{\rm UV}$ as a function of redshift for our spec-z-confirmed sources, together with the photometric and spectroscopic sample in the literature at $z\gtrsim8$. Owing to the deep survey layer efficiently explored by the gravitationally lensing effect, our UNCOVER sources increase the sample in the high-redshift ($z\gtrsim9$) and faint ($M_{\rm UV}\lesssim-19$) regime by a factor of 3.

3.2. z_{phot} versus z_{spec}

In the left panel of Figure 5, we compare the $z_{\rm phot}$ and $z_{\rm spec}$ estimates for the spec-z-confirmed sources. For the four sources presented in Atek et al. (2023b, A23 hereafter; red filled circles), we adopt the $z_{\rm phot}$ estimates from A23 with the 1σ error range. For the other six sources (red open circles), we use the $z_{\rm phot}$ estimates from the `eazy` fitting with the default `corr_sfhz_13` template set (B. Wang et al. 2024). For the latter six sources, we show the 2σ error range, given the nonhomogeneous selection criteria adopted in the MSA target selection process (Section 2.2). We find that all $z_{\rm phot}$ estimates agree with $z_{\rm spec}$ within the $\sim$1–2σ error ranges. Among the sources presented in A23, there are no other sources included in our MSA design apart from the four sources, resulting in the success ratio of the spec-z confirmation being 100% (=4/4) for the A23 sample. This high confirmation rate is consistent with previous systematic NIRSpec follow-up studies for NIRCam-selected high-redshift candidates at $z\gtrsim9$ in the CEERS survey ($\simeq$90%; P. Arrabal Haro et al. 2023b; S. Fujimoto et al. 2023c), validating the classical high-redshift galaxy selections based on the $z_{\rm photo}$ estimates and/or the dropout technique. Interestingly, the A23 sample shows the offset of the redshift $\Delta z(\equiv z_{\rm phot}-z_{\rm spec})\in[-0.4,+0.4]$, which is in contrast to the previous NIRSpec follow-up studies showing a trend of the overestimate in $z_{\rm phot}$ typically $\Delta z\simeq+0.5$ and maximally $\sim$+1–2, regardless of the choice of the $z_{\rm phot}$ estimates from different literature (P. Arrabal Haro et al. 2023b; S. Fujimoto et al. 2023c; K. N. Hainline et al. 2024). The overestimate of $z_{\rm phot}$ is likely because of the softened Lyα-break shape routinely identified in the NIRSpec spectra for high-redshift galaxies with possible causes of the IGM Lyα absorption, the intrinsic SED shape, and/or the additional damped Lyα absorber (DLA) systems (e.g., P. Arrabal Haro et al. 2023b; E. Curtis-Lake et al. 2023; K. E. Heintz et al. 2024; T. Y.-Y. Hsiao et al. 2024; H. Umeda et al. 2024). In addition to the deep NIRCam blue (F115W and F150W) filters taken in UNCOVER ($5\sigma\simeq30$ mag) that are deeper than those taken in CEERS by $\simeq$1 mag (S. L. Finkelstein et al. 2023), one of the most strict selection criteria is adopted in the A23 selection, including the sharp Lyα-break color of $>$1.5 mag and the consistent redshift solutions from different SED fitting codes. The presence of the deep blue filters and the strict sample selection may be plausible reasons that mitigate the overestimation of $z_{\rm phot}$ in the A23 sample.

3.3. z_{line} versus z_{break}

Among our spec-z-confirmed sources, some are detected with multiple emission lines, making their $z_{\rm spec}$ estimates very secure. On the other hand, others without the multiple emission-line detection mainly rely on the Lyα break feature, which may still have uncertainty in their $z_{\rm spec}$ estimates. Motivated by this, we compare the line-based redshift estimate ($z_{\rm line}$) and the Lyα-break-based redshift estimate ($z_{\rm break}$). We use ID20466, ID10646, ID3686, ID22223, ID26185, and ID13151, which show multiple emission-line detections (Figure 3) and are suitable for this experiment. For $z_{\rm line}$, we mask the ±0.1 μm range from the observed Lyα wavelength in the 1D spectra. For $z_{\rm break}$, we mask all wavelengths with $\lambda\geqslant3.0$ μm and the ±0.05 μm ranges from the observed wavelengths of detected emission lines in the 1D spectra. We then rerun the same template fitting to the masked spectra as Section 3.1 and derive $z_{\rm line}$ and $z_{\rm break}$.

In the right panel of Figure 5, we compare our $z_{\rm line}$ and $z_{\rm break}$ estimates. We find that the offset between the line and Lyα-break-based redshifts $\Delta z'(\equiv z_{\rm line}-z_{\rm break})\in[-0.2,+0.2]$. This indicates that the redshift estimate based on the Lyα break feature alone may still have the uncertainty of ±0.2. Given that we perform this experiment only with the sources with multiple significant emission-line detections, which are mostly equal to the best SNR spectra, the offset could be even worse than ±0.2 with lower SNR data. This is important for the design of future follow-up spectroscopy based on the redshift estimates with NIRSpec/prism, especially when using

Table 1
Summary of Spectroscopically Confirmed Sources at $z \geqslant 8.5$ in UNCOVER

ID	R.A. (deg)	Decl. (deg)	$z_{\rm spec}$	F200W (mag)	F444W (mag)	μ	$M_{\rm UV}$	Spec. Feature	$T_{\rm exp.}$ (hr)	Photo Ref.	Spec Ref.	AGN?
(1)	(2)	(3)	(4)	(5)	(6)	(7)	(8)	(9)	(10)	(11)	(12)	
20466	3.640408393	−30.38643761	$8.500^{+0.000}_{-0.001}$	28.47	26.20	$1.3^{+0.0}_{-0.0}$	−18.11	Break, Line	2.7 (2)	L23	This	Y[a]
10646	3.636959984	−30.40636156	$8.511^{+0.000}_{-0.001}$	25.35	24.09	$1.4^{+0.0}_{-0.0}$	−21.56	Break, Line	2.7 (2)	⋯	This	Y/N[b]
3686	3.617202003	−30.42553381	$9.325^{+0.000}_{-0.001}$	25.12	25.08	$1.6^{+0.0}_{-0.0}$	−21.72	Break, Line	2.7 (2)	A23, C23	B23, This	Y/N
22223	3.568114512	−30.38305164	$9.568^{+0.000}_{-0.001}$	28.68	28.74	$3.9^{+0.3}_{-0.1}$	−17.28	Break, Line	4.4 (4)	⋯	This	N
31028	3.544169292	−30.37031863	$9.740^{+0.000}_{-0.001}$	27.46	27.48	$6.7^{+0.1}_{-1.5}$	−17.85	Break	6.9 (3, 6)	⋯	This	N
13151	3.592501339	−30.40146429	$9.880^{+0.012}_{-0.001}$	27.05	27.38	$12.8^{+0.6}_{-0.8}$	−17.63	Break, Line	11.8 (5, 6, 7)	Z14	RB23, This	N
26185	3.567070796	−30.37786065	$10.071^{+0.000}_{-0.001}$	27.09	27.17	$3.9^{+0.5}_{-0.1}$	−18.93	Break, Line	7.1 (1, 4)	A23, C23	G23, This	Y[c]
37126	3.590110772	−30.35974219	$10.255^{+0.001}_{-0.001}$	26.85	27.41	$1.8^{+0.0}_{-0.1}$	−20.01	Break	6.9 (3, 4)	A23	This	N
38766	3.513563316	−30.35679963	$12.393^{+0.004}_{-0.001}$	28.17	28.46	$1.5^{+0.0}_{-0.0}$	−19.17	Break	4.4 (4)	A23	W23, This	N
13077	3.570869325	−30.40158533	$13.079^{+0.014}_{-0.001}$	27.73	28.82	$2.3^{+0.0}_{-0.1}$	−19.24	Break	7.4 (5, 7)	⋯	W23, This	N

Notes. (1) Source ID used in MSA. We also describe the ID used in the photometric catalog (J. R. Weaver et al. 2024) in Appendix A. (2)–(3) Source coordinate. (4) Spectroscopic redshift ($z_{\rm spec}$) determined by our SED template fitting method (see text). (5)–(6) Total magnitude in NIRCam F200W and F444W filters, respectively, measured in J. R. Weaver et al. (2024). (7) Magnification factor based on $z_{\rm spec}$ and the latest lens model, including eight more multiple image systems spectroscopically confirmed in the UNCOVER NIRSpec observations (L. J. Furtak et al. 2023b). (8) Absolute UV magnitude, calculated with the total flux in the NIRCam F150W and F200W filters for the sources at $z_{\rm spec} = 8.5$–10 and $z_{\rm spec} > 10$, respectively. (9) Key spectroscopic features observed in the prism that critically determine the source redshift in our method. "Line" denotes the sources with multiple line detections. (10) Exposure time in hours. The MSA IDs are also denoted in parentheses. (11)–(12) Reference for photometric and/or spectroscopic results (L23: I. Labbe et al. 2023b; A23: H. Atek et al. 2023b; B23: K. Boyett et al. 2024; C23: M. Castellano et al. 2023; RB23: G. Roberts-Borsani et al. 2023; G23: A. D. Goulding et al. 2023; W23: B. Wang et al. 2023a; and Z14: A. Zitrin et al. 2014). The IDs in the literature are summarized in Appendix B. (13) AGN or not. "Y" indicates an AGN, while "N" indicates no evidence of AGN has been observed in the current data. "Y/N" represents the potential AGN sources implied from the emission-line properties in prism (Section 3.1) and UV LF measurements (Section 4).

[a] From the BL identification in Hβ (see more details in V. Kokorev et al. 2023). ID13556 in I. Labbe et al. (2023b).

[b] See more details in J. Weaver et al. (2024, in preparation) for line diagnostics and contributions from AGN and star-forming activities.

[c] Recent deep 1.25 Ms Chandra observations show a 4.2σ detection of ID26185 (A. Bogdan et al. 2024; see also A. D. Goulding et al. 2023).

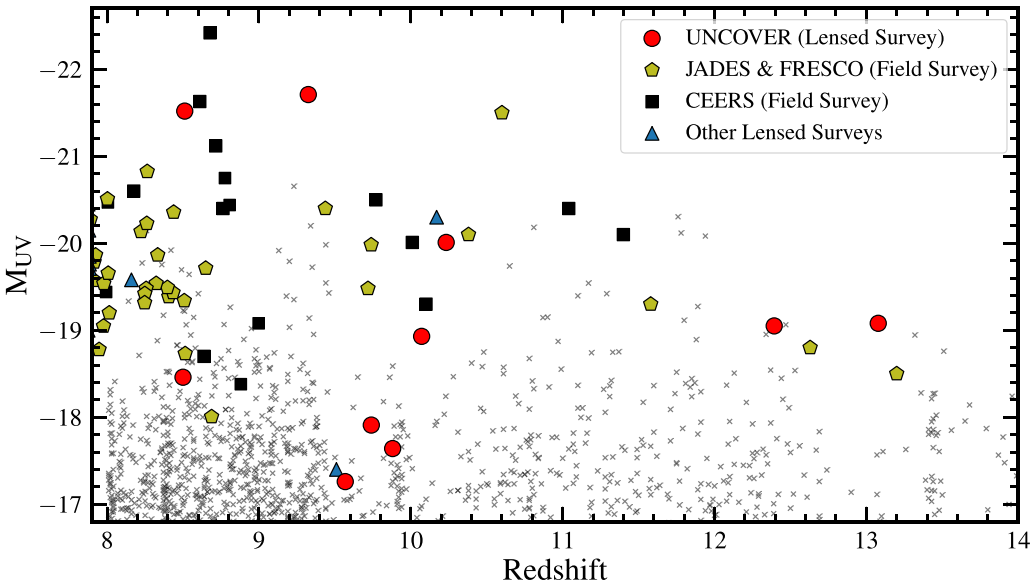

Figure 4. Redshift vs. M_{UV}. The magnification correction is applied for the lensed sources. The red circles represent our spec-z-confirmed sources in UNCOVER at $z \geqslant 8.5$, efficiently increasing the sample at the faint ($M_{UV} \gtrsim -19$) and high-redshift ($z \gtrsim 9.5$) regime. The gold pentagons and the black squares show recent JWST spectroscopic results from other field surveys such as JADES (e.g., A. J. Bunker et al. 2023), FRESCO (e.g., P. A. Oesch et al. 2023), and CEERS (e.g., S. L. Finkelstein et al. 2023), where the values are taken from K. N. Hainline et al. (2024). The blue triangles denote recent JWST/NIRSpec observation results for high-redshift lensed galaxies (C. C. Williams et al. 2023; T. Y.-Y. Hsiao et al. 2024). The gray crosses indicate the photometric candidates with NIRCam publicly available in JADES v1.0 catalog (K. N. Hainline et al. 2024).

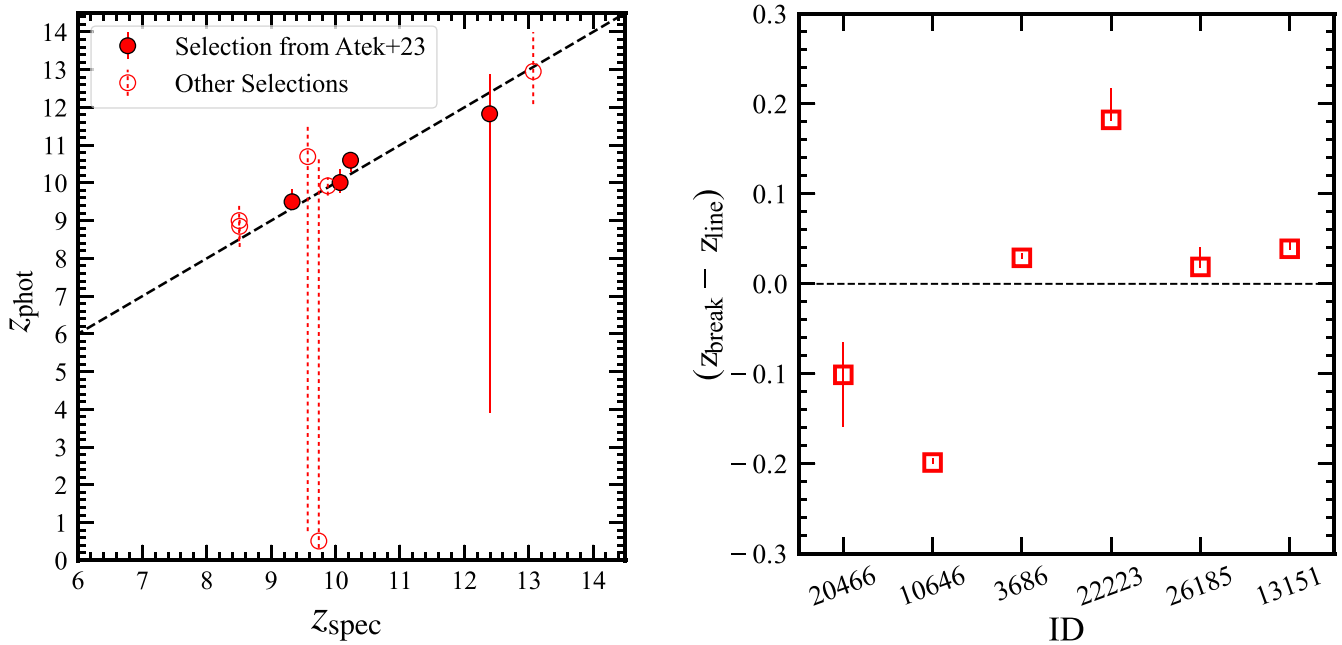

Figure 5. Left: comparison between z_{phot} and z_{spec} for our spec-z-confirmed sources. The red filled and open circles represent the sources selected from A23 and other selections, respectively (see Section 3.1). The error bars show the 1σ error range for the A23 sample, while the other sources show the 2σ error range given the nonhomogeneous selection criteria adopted in the MSA target selection process (Section 2.2). Right: comparison between the redshift estimates based on lines (z_{line}) and the Lyα break (z_{break}) for six sources whose multiple emission lines are successfully detected in the prism spectrum. Two sources (ID20466 and ID10646) show $z_{break} - z_{line} < -0.1$, indicating the presence of the nonzero fluxes blueward of the Lyα emission in the prism spectra and the ionized bubbles around these two sources (Section 5).

instruments whose redshift coverage of targeting emission lines can be narrower than this potential redshift uncertainty, such as the Atacama Large Millimeter/submillimeter Array (ALMA).

Individually, ID22223 shows z_{break} overestimated by $\sim$0.2. The 1D spectrum clearly shows the softened shape of the Lyα break, which is the natural cause of the overestimate of z_{break}. ID3686, ID26185, and ID13151 also show slight overestimates in z_{break} ($\Delta z' < 0.05$). In the 1D spectra of these three sources, we identify a softened shape in the Lyα break more or less similar to that of ID22223. These results indicate that the slight overestimate of z_{break} in these three sources is also caused by the similar softened shape of the Lyα break, while the clear cutoff of the Lyα break mitigates the effect. Therefore, an overestimation of z_{break} does not always severely occur due to

the softened Lyα break, depending on the SNR of the spectrum.

In ID20466 and ID10646, on the other hand, the $z_{\rm break}$ values are underestimated by $\sim$0.1–0.2. Their 1D spectra show that the Lyα line and continuum continue down to shorter wavelengths than rest-frame 1216 Å, indicative of an enhanced transmission of the Lyα line and continuum due to the presence of the so-called proximity zone, which has been often observed around high-redshift luminous quasars (e.g., A.-C. Eilers et al. 2017). We further discuss the proximity zone around ID20466 and ID10646 in Section 5.

4. Ultraviolet Luminosity Function at $z \gtrsim 9$ and Implications of Active Galactic Nucleus Contributions

4.1. Ultraviolet Luminosity Function from UNCOVER

We calculate the UV LFs at $z \gtrsim 9$ using our spec-z-confirmed sources. Note that we could not assign all the $z \gtrsim 9$ photometric candidates slits in the MSA design, and thus our measurements provide only the lower limits. In the same manner as Y. Harikane et al. (2024), we divide our sample into three redshift bins at $z_{\rm spec} = 8.5$–9.5, 9.5–11.0, and 11.0–13.5. To simplify the calculation, we adopt a top-hat function for the volume calculation according to the redshift bin. For the survey area, since the MSA footprints are restricted to the high-priority targets originally identified from the NIRCam observation around the primary and two subcluster regions in A2744, we use the NIRCam mosaic for the primary UNCOVER area ($\sim$28 arcmin^2; R. Bezanson et al. 2024) and obtain the effective survey area by applying the magnification correction in the same manner as A23. Note that two objects (ID3686 and ID10646) slightly outside the primary UNCOVER area still fall within our MSA footprint near the edge. However, including all outside NIRCam areas taken in other programs (e.g., GLASS) would be inappropriate as most are not covered by our MSA footprint due to the restriction. Additionally, our MSA footprint does not cover about 40% of the primary UNCOVER area itself. Given these factors, using the 28 arcmin^2 area provides a reasonable balance for our survey volume estimation. The uncertainty is calculated from Poisson errors with the values presented in N. Gehrels (1986), where we take cosmic variance into account, following A. C. Trapp & S. R. Furlanetto (2020). No completeness correction is applied, which makes our lower limit estimates conservative. Our full UV LF measurements using the photometric sample leveraged by the success ratio of the spec-z confirmation are presented in I. Chemerynska et al. (2024).

The left panel of Figure 6 shows our UV LF measurements for galaxies (red circles; $N = 8$) and AGNs (magenta pentagons; $N = 2$). For comparison, we also present the previous photometric UV LF measurements (gray squares) taken from the literature (D. J. McLeod et al. 2016; T. Morishita et al. 2018; P. A. Oesch et al. 2018; M. Stefanon et al. 2019; R. A. A. Bowler et al. 2020; R. J. Bouwens et al. 2022; M. Castellano et al. 2022; S. L. Finkelstein et al. 2022a, 2022b; R. P. Naidu et al. 2022b; R. Bouwens et al. 2023a; C. T. Donnan et al. 2023; Y. Harikane et al. 2023a; N. Leethochawalit et al. 2023; G. C. K. Leung et al. 2023; T. Morishita & M. Stiavelli 2023; P. G. Pérez-González et al. 2023; M. B. Bagley et al. 2024; M. Franco et al. 2024) and the best-fit Schechter function (black curve) presented in P. G. Pérez-González et al. (2023). We also show two bright JWST-observed sources, GNz11 and CEERS1019, which are argued to be AGNs in the literature (e.g., R. L. Larson et al. 2023; R. Maiolino et al. 2024c). For GNz11, we calculate the survey area with the entire CANDELS field (736 arcmin^2; R. J. Bouwens et al. 2022). For CEERS1019, we calculate the survey area from the CANDLES fields of GOODS-N, Extended Groth Strip, Ultra Deep Survey, and COSMOS, where the original spectroscopic sample was selected (R. L. Larson et al. 2022). For volume calculations, we assume $\Delta z = 1.0$ in the same manner as P. A. Oesch et al. (2018) for both sources. The uncertainty is estimated by the Poisson error and the cosmic variance.

We find that our measurements for both galaxies and AGNs are consistent with the previous photometric measurements, except for the brightest $M_{\rm UV}$ bin in the $z \sim 9$ UV LF. This exceptional data point consists of our two brightest sources, ID3686 at $z = 9.33$ and ID10646 at $z = 8.51$. These two sources are located at different redshifts, indicating that the excess from the previous UV LF measurements is not caused by an overdensity but by their uniquely UV-bright properties. Interestingly, both of these sources show some implications as AGNs from the identification of high-ionization emission lines such as N IV] λ1749, C IV λ1549, and He II λ1640 and the uniquely high [O III] λ5008/Hβ ratio of $>$10 (Section 3.1). Although both of these sources are spatially resolved in the NIRCam filters, many BL AGNs have been identified in spatially resolved sources in recent NIRSpec studies (e.g., Y. Harikane et al. 2023b; R. L. Larson et al. 2023). Even if the AGN contribution to the total UV luminosity is 50%, the $M_{\rm UV}$ value moves toward the bright end by $\sim$0.7 mag, which may easily impact the bright-end shape of the UV LF. These UV LF measurements offer another independent implication of the potential AGN nature of these UV-brightest sources.

In the left panel of Figure 6, we also show the AGN LF estimated at $z \sim 6$ for X-ray AGNs (the magenta dashed line; E. Giallongo et al. 2019). This X-ray AGN LF shows an excellent agreement with the lower boundaries obtained from the BL AGN of ID20466 at $z = 8.50$ and the X-ray-luminous AGN (ID26185) at $z = 10.07$. This indicates that a comprehensive AGN LF at $z \gtrsim 9$ could have a comparable, even higher amplitude than the previous measurement at $z \sim 6$. We summarize our lower limit constraints on the UV LFs of galaxies and AGNs in Tables 2 and 3, respectively.

4.2. Ultraviolet Luminosity Function from UNCOVER + CEERS + JADES

To benefit from the complementary survey layers enabled by the lensing cluster surveys and the general field surveys, we also evaluate the UV LF together with public spec-z-confirmed sources at $z \geqslant 8.5$ in recent JWST/NIRSpec MSA studies (e.g., P. Arrabal Haro et al. 2023a, 2023b; A. J. Bunker et al. 2023, 2024; S. Fujimoto et al. 2023c; Y. Harikane et al. 2023b; M. Tang et al. 2023; K. N. Hainline et al. 2024; T. Y.-Y. Hsiao et al. 2024). We include the sources spectroscopically confirmed at $z \geqslant 8.5$ in two general field surveys of CEERS (e.g., P. Arrabal Haro et al. 2023b; S. L. Finkelstein et al. 2023; S. Fujimoto et al. 2023a) and JADES in GOODS-S (hereafter JADES-GS; e.g., E. Curtis-Lake et al. 2023; B. E. Robertson et al. 2023; A. J. Bunker et al. 2024; K. N. Hainline et al. 2024) with our spectroscopically confirmed sources in UNCOVER. We also use the sources spectroscopically confirmed in a JWST DDT follow-up observation with NIRSpec/prism MSA, which primarily aims to confirm a remarkably UV-bright galaxy

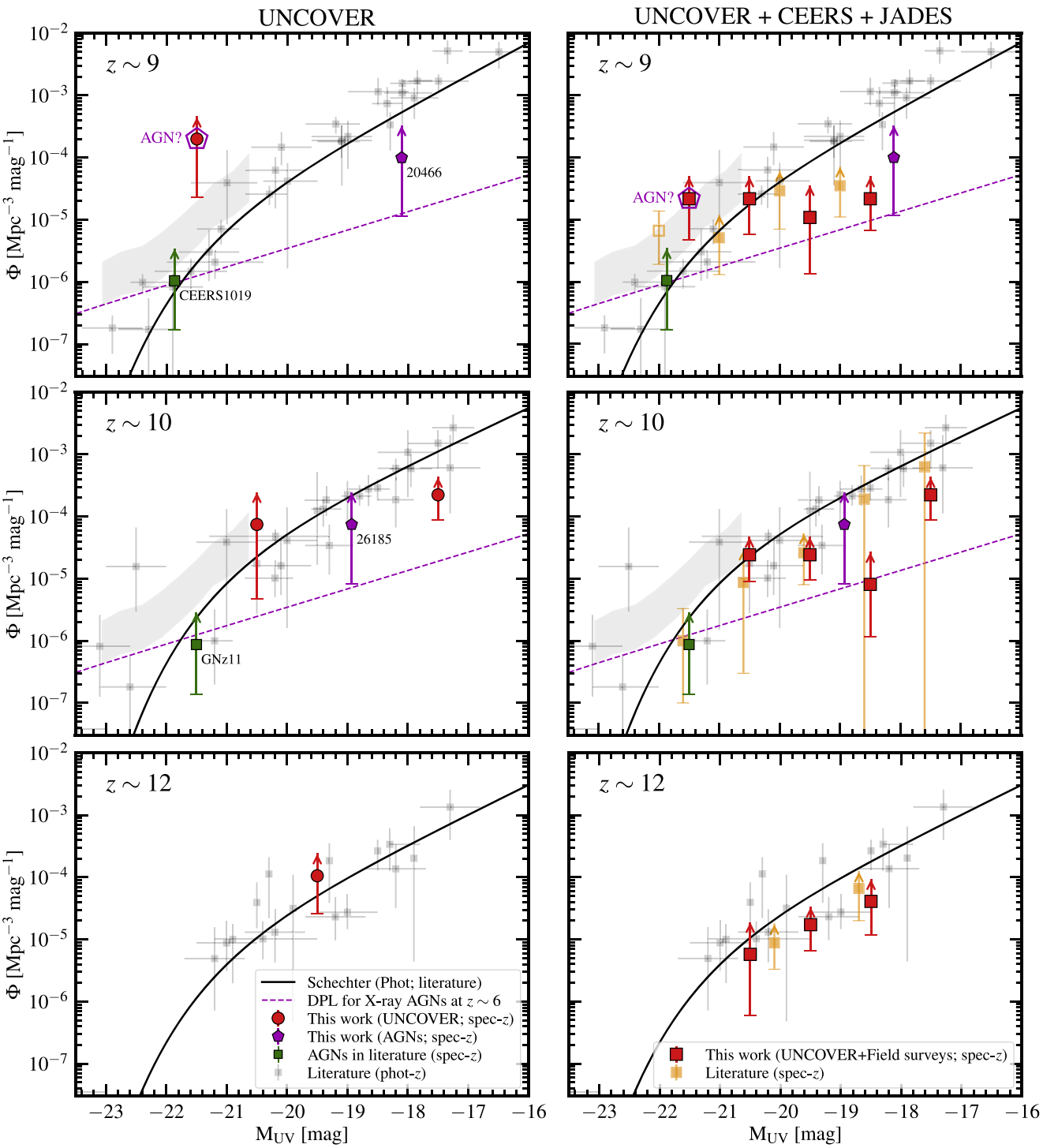

Figure 6. Constraints on the UV LF at $z \sim 9$, $z \sim 10$, and $z \sim 12$. The magenta pentagons represent the AGN sources from BL (ID20466) and X-ray (ID26185) detections, and the red circles present the other eight sources in our spec-z-confirmed sample in UNCOVER. The red squares denote the spec-z-confirmed nonobvious AGN sources from UNCOVER, CEERS, and JADES GOODS-S, where we do not include several sources in the $z = 8.7$ overdensity reported in the CEERS field (see text). The gray shaded region and gray squares show the previous photometric measurements, and the black solid curve denotes the best-fit Schechter function estimated in P. G. Pérez-González et al. (2023). The orange squares show the recent spectroscopic measurements (Y. Harikane et al. 2023b). The green squares denote the recent JWST-observed bright objects of GNz11 (R. Maiolino et al. 2024b) and CEERS1019 (R. L. Larson et al. 2023) reported as AGNs. The magenta dashed curve presents the best-fit double power-law function for $z \sim 6$ AGNs (E. Giallongo et al. 2019). The open magenta pentagon remarks the two possible AGN sources at different redshifts that show uniquely high-ionization emission lines such as N IV] λ1749, C IV λ1549, and He II λ1640 (ID10646 at $z = 8.51$) and high [O III] λ5008/Hβ ratio of >10 (ID3686 at $z = 9.33$), where the excess is not caused by an overdensity but by their uniquely UV-bright properties.

candidate at $z \sim 16$ (P. Arrabal Haro et al. 2023a). We obtain 12 and seven spec-z-confirmed sources from CEERS (+DDT) and JADES-GS, respectively, covering a wide M_{UV} range of $\in$ [–22.2, –18.0]. In conjunction with our UNCOVER sample, our final spec-z sample in this analysis results in a total number of 29.

Table 2
Spectroscopic Constraints on $z \simeq 9$–12 Ultraviolet Luminosity Functions

$M_{\rm UV}$ (AB mag)	Φ (UNCOVER) (10^{-5} Mpc^{-3} dex^{-1})	Φ (UNCOVER + Fields) (10^{-5} Mpc^{-3} dex^{-1})
(1)	(2)	(3)
	$z \sim 9$	
−21.5	$>19.9^{+25.9}_{-17.6}$	$>2.16^{+2.81}_{-1.69}$
−20.5	⋯	$>2.16^{+2.81}_{-1.59}$
−19.5	⋯	$>1.08^{+2.49}_{-0.95}$
−18.5	⋯	$>2.16^{+2.81}_{-1.49}$
	$z \sim 10$	
−20.5	$>7.45^{+17.1}_{-6.98}$	$>2.43^{+2.34}_{-1.53}$
−19.5	⋯	$>2.43^{+2.34}_{-1.47}$
−18.5	⋯	$>0.81^{+1.86}_{-0.69}$
−17.5	$>22.4^{+21.6}_{-13.5}$	$>22.4^{+21.6}_{-13.5}$
	$z \sim 12$	
−20.5	⋯	$>0.69^{+1.58}_{-0.62}$
−19.5	$>10.6^{+13.8}_{-7.88}$	$>2.06^{+1.99}_{-1.27}$
−18.5	⋯	$>4.08^{+5.31}_{-2.90}$

Note. (1) Absolute UV magnitude. (2) UV LF constraints with spec-z-confirmed sources in UNCOVER, except for two AGNs (see text), resulting in $N = 8$. (3) UV LF constraints with spec-z-confirmed sources in UNCOVER, CEERS, and JADES, except for two AGNs (R. L. Larson et al. 2023; R. Maiolino et al. 2024b) and the sources in the $z = 8.7$ overdensity in the CEERS field reported in the literature (R. L. Larson et al. 2022), resulting in $N = 23$. Errors and upper limits are 1σ, evaluated with Poisson uncertainties (N. Gehrels 1986) and cosmic variance (A. C. Trapp & S. R. Furlanetto 2020).

Table 3
Spectroscopic Constraints on $z \simeq 9$–10 Active Galactic Nucleus Luminosity Functions

Redshift	$M_{\rm UV}$ (AB mag)	Φ (AGN) (10^{-5} Mpc^{-3} dex^{-1})
$z \sim 9$	−18.1	$>9.96^{+22.9}_{-8.81}$
$z \sim 10$	−18.9	$>7.45^{+17.1}_{-6.63}$

Note. Same as Table 2, but for the AGN LFs constrained from two spec-z-confirmed AGNs of ID20466 and ID26185.

We calculate the survey volume as follows. In JADES-GS, the NIRSpec observations had small dithers ($<1''$) with one pointing, and the NIRSpec pointing center was not reoptimized to the late addition of the high-priority NIRCam sources (A. J. Bunker et al. 2024). Therefore, we regard the JADES-GS NIRSpec observations as a pure general field survey almost with a single NIRSpec pointing and adopt the NIRSpec FOV of 9 arcmin^2.[34] In CEERS, the NIRSpec observations were initially designed with six pointings, where one pointing was added from the DDT NIRSpec observations (#2750: PI: P. Arrabal-Haro; P. Arrabal Haro et al. 2023b) for the $z \sim 16$ candidate (C. T. Donnan et al. 2023). Among the original six pointings in CEERS, the prism observations in two pointings were affected by an electrical short and thus rescheduled (P. Arrabal Haro et al. 2023b). Although the pointing centers of the rescheduled two NIRSpec observations were optimized to maximize the yield of the NIRCam-selected high-redshift galaxy candidates, we assume that the potential bias from this optimization for the targets is insignificant, given the ratio to the total number of the pointings (=2/9, $\lesssim$20%). Since the primary target in the DDT observation is the $z \sim 16$ candidate, we assume that the potential bias in the DDT observation for other $z \gtrsim 9$ galaxies within the NIRSpec FOV is also minimal. In a similar manner as Y. Harikane et al. (2024), we count the area overlapped between the FOVs of the NIRSpec and NIRCam in CEERS and obtain 37.5 arcmin^2. We add the survey areas from JADES-GS and CEERS to that of UNCOVER, and rederive the UV LFs with three redshift bins at $z_{\rm spec} = 8.5$–9.5, 9.5–11.0, and 11.0–13.5. We do not include CEERS-D28 at $z = 8.763$, CEERS1025 at $z = 8.715$, CEERS1019 at $z = 8.679$, CEERS80083 at $z = 8.638$, and CEERS1029 at $z = 8.610$ (P. Arrabal Haro et al. 2023b) in our estimates, as the $z = 8.7$ overdensity has been reported in the literature (e.g., R. L. Larson et al. 2022; M. Castellano et al. 2023; Y. Harikane et al. 2023b).

In the right panel of Figure 6, we present the UV LF measurements with the spec-z-confirmed sources in UNCOVER, CEERS, and JADES. For comparison, we also present the recent NIRSpec spec-z-based measurements (the orange squares; Y. Harikane et al. 2023b). We confirm that our measurements are generally consistent with the previous spec-z-based measurements and improve the lower constraints owing to the comprehensive spec-z sample, including the lensing cluster and general field surveys. We find that the brightest $M_{\rm UV}$ bin in the $z \sim 9$ UV LF still shows an excess from the previous photometric UV LF measurements beyond the errors, which still consists of ID10646 and ID3686. This indicates that the excess is unlikely explained by cosmic variance. A similar excess has also been reported in recent JWST studies (e.g., M. Castellano et al. 2023; Y. Harikane et al. 2023b), and this has been interpreted as a galaxy overdensity. However, we do not include the sources in the $z = 8.7$ overdensity (R. L. Larson et al. 2022) in our measurements. Besides, ID3686 and ID10646 are at different redshifts. Thus, the excess is more likely caused by their uniquely UV-bright properties than the excess in abundance, offering independent implications that they are the AGNs, as discussed in Section 4.1. In Table 3, we also summarize the UV LF measurements using the spec-z sources from UNCOVER, CEERS, and JADES.

4.3. Comparison with Models

We compare our UV LF measurements with theoretical predictions. In Figure 7, we show theoretical predictions of the UV LF at $z \sim 9$, $z \sim 10$, and $z \sim 12$, together with our UV LF measurements using the spec-z-confirmed sources in UNCOVER, CEERS, and JADES. We find that our lower limit estimate in the brightest $M_{\rm UV}$ bin challenges some theoretical predictions in every redshift range. This indicates that we confirm the earlier reports of the high abundance of UV-bright ($M_{\rm UV} \lesssim -20$) galaxies argued in the photometric studies (e.g., H. Atek et al. 2023a, 2023b; M. Castellano et al. 2022; S. L. Finkelstein et al. 2022b, 2023; R. P. Naidu et al. 2022b; N. J. Adams et al. 2023; D. Austin et al. 2023; R. J. Bouwens et al. 2023b; L. D. Bradley et al. 2023; C. T. Donnan et al. 2023; Y. Harikane et al. 2023a; I. Labbe et al. 2023a; G. C. K. Leung et al. 2023; T. Morishita & M. Stiavelli 2023; C. C. Williams et al. 2023; H. Yan et al. 2023) in a spectroscopic manner at $z \sim 9$–12. Several possible

[34] https://jwst-docs.stsci.edu/jwst-near-infrared-spectrograph#gsc.tab=0

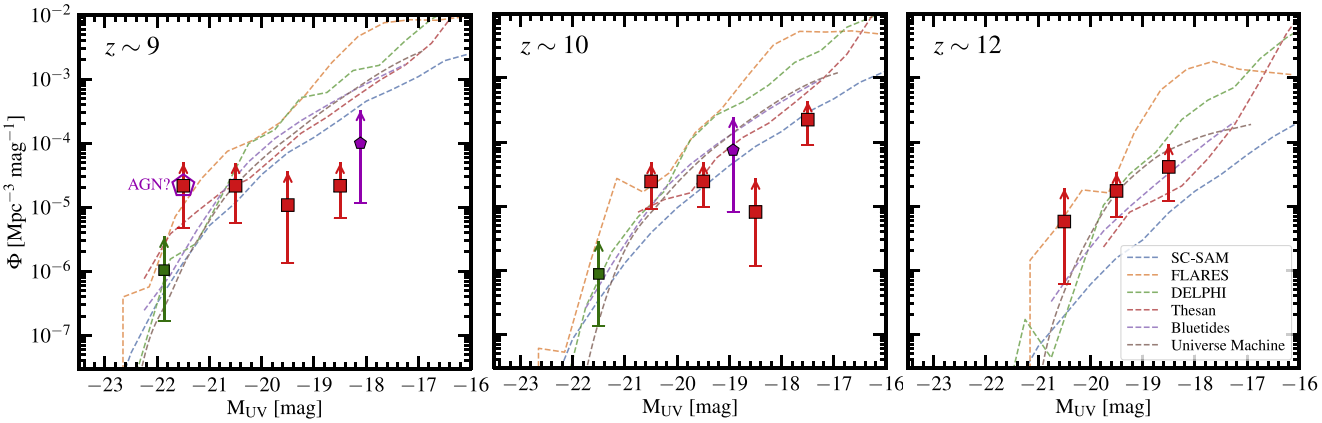

Figure 7. Comparison of the LFs with the theoretical predictions in the literature at $z \sim 9$, $z \sim 10$, and $z \sim 12$. The symbols are the same as Figure 6, The color dashed lines denote the theoretical predictions of SC-SAM (L. Y. A. Yung et al. 2019), FLARES (A. P. Vijayan et al. 2021; C. C. Lovell et al. 2023; S. M. Wilkins et al. 2023), DELPHI (P. Dayal et al. 2014; V. Mauerhofer & P. Dayal 2023), Thesan (R. Kannan et al. 2023), Bluetides (S. M. Wilkins et al. 2017), and Universe Machine (P. Behroozi et al. 2020). In each redshift range, our lower limit estimate in the brightest M_{UV} challenges several theoretical predictions, confirming the earlier arguments of the high abundance of UV-bright ($M_{UV} \lesssim -20$) galaxies in previous photometric studies in a spectroscopic manner at $z \sim 9$–12.

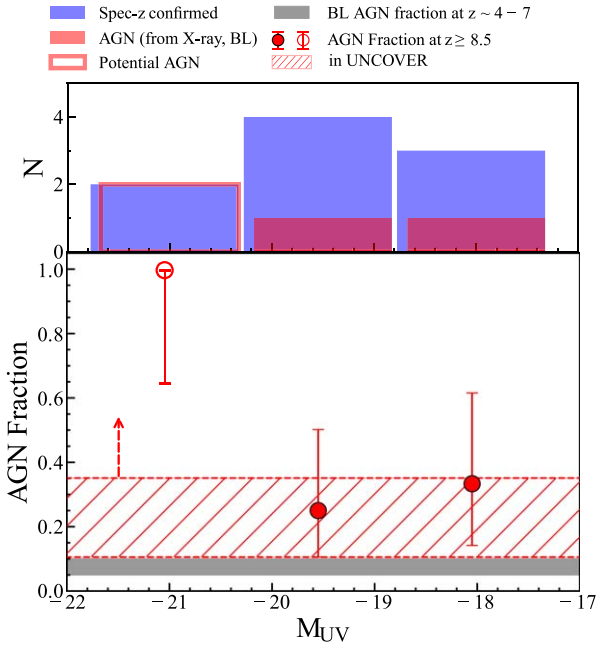

Figure 8. AGN fraction at $z \geqslant 8.5$. The blue and red histograms present the number of AGNs and the sources that are spectroscopically confirmed in our studies at each M_{UV} bin. The histogram with a red outline represents the two possible AGN sources of ID10646 and ID3686 that fall in the brightest M_{UV} bin. The red circles indicate the AGN fraction for the spec-z-confirmed UNCOVER sources at $z \geqslant 8.5$, where we show the brightest M_{UV} bin in the case that both AGN candidates are truly AGNs. The error bars represent the confidence intervals for the binomial proportion, derived using the Jeffreys interval at 1σ. The red hatched area shows the 1σ range for the AGN fraction over the entire M_{UV} range (=2/10). This may be a lower limit, as more sources, including ID10646 and ID3686, might be confirmed to be AGNs in future observations. The black shaded area denotes the recent reports of $\simeq$5% −10% BL AGN fractions from the BL AGN identifications in recent NIRSpec studies at $z \simeq 4$–7 (Y. Harikane et al. 2024; R. Maiolino et al. 2024a).

scenarios for the high abundance have been discussed, including preferential detection of galaxies up-scattered compared to the main sequence, lower dust attenuations with increasing redshift, a top-heavy IMF, or even UV luminosity contribution from an AGN component (e.g., K. Inayoshi et al. 2022; R. P. Naidu et al. 2022b; F. Pacucci et al. 2022; R. Bouwens et al. 2023a; A. Ferrara et al. 2023; S. L. Finkelstein et al. 2023; Y. Harikane et al. 2023b). Given that the most stringent lower limit obtained at $z \sim 9$ is dominated by possible AGN sources (Sections 4.1 and 4.2), it seems increasingly plausible that the bright end of the UV LF is shaped by sources where the UV luminosity is contributed by both star formation and black hole accretion. Although further observational evidence is necessary to conclude whether those possible sources are truly AGNs or not, such observations will prove crucial in baselining theoretical models and shedding light on black hole seeding and growth at these early epochs.

4.4. Active Galactic Nucleus Fraction

We investigate the AGN fraction at $z \geqslant 8.5$. Note that here we count the spec-z-confirmed sources in UNCOVER alone, since homogeneous data and sensitivity are required to examine the AGN fraction. Figure 8 presents the AGN fraction as a function of M_{UV} from our spec-z sample. We calculate the 1σ uncertainty from the confidence intervals for the binomial proportion, derived using the Jeffreys interval. The red hatched area indicates the 1σ range of the AGN fraction over the entire M_{UV} range with our secure AGNs from the BL and X-ray detections (=2/10), while we also show the possible AGN fraction in the brightest M_{UV} bin, which consists of the possible AGN sources of ID10646 and ID3686. For comparison, we also show the BL AGN fraction of ≈5%–10% estimated at $z \simeq 4$–7 in recent JWST/NIRSpec studies (Y. Harikane et al. 2024; R. Maiolino et al. 2024a).

We find that our results suggest a relatively high AGN fraction of >10%–35% compared to the previous measurements from the BL AGNs. Although a potential bias in the MSA target selection might exist (e.g., robust photo-z sources), our higher AGN fraction than the previous measurements can be interpreted as a more comprehensive approach adopted in the AGN identification than the BL identification alone. Since weak-line quasars have also been identified at $z > 6$ (e.g., I. T. Andika et al. 2020; S. Fujimoto et al. 2022), the BL approach can be hampered by observational bias for those sources whose BL EW is high (≈high M_{BH}/M_{star}) and/or

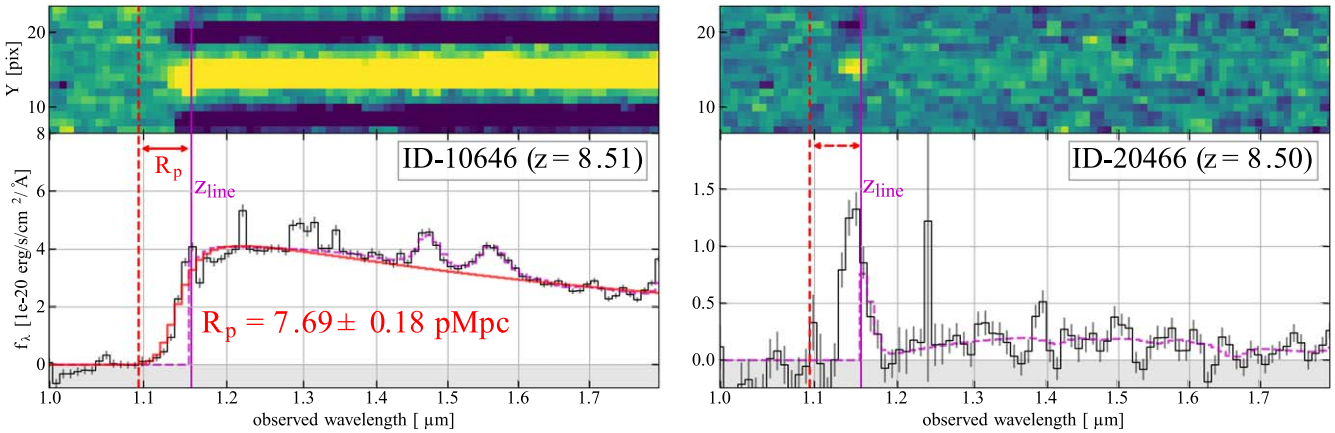

Figure 9. Zoom-in 1D + 2D prism spectra of ID10646 (left) and ID20466 (right). The magenta vertical line and dashed curve indicate the expected Lyα line wavelength and the best-fit spline model using `msaexp` based on $z_{\rm line}$, respectively. Blueward of the Lyα continuum or line is clearly detected in both sources. The red curve in ID10646 represents our best-fit IGM absorbed model with an ionized bubble, yielding a best-fit $R_{\rm p}$ value of 7.69 ± 0.18 pMpc. The red vertical line corresponds to the expected wavelength of the Lyα line based on the redshift of the ionization front of the ionized bubble along the line of sight. Because of the lack of the blueward Lyα continuum and the difficulty in modeling the intrinsic Lyα line profile in ID20466, we perform the $R_{\rm p}$ measurement only for ID10646. For reference, the red dashed vertical line in ID20466 is drawn at the same wavelength as the red vertical line in the left panel.

whose BL width is sufficiently broad (≈more massive $M_{\rm BH}$) to be resolved with JWST instruments. On the other hand, in addition to the successful identification of the BL AGN at $z = 8.50$, we identify the X-ray-luminous AGN at $z = 10.07$ and several potential AGN sources from multiple angles, owing to the deep NIRSpec/prism spectroscopy leveraged by the lensing effect and the ancillary deep X-ray data (e.g., A. Bogdan et al. 2024). Although further observational evidence is necessary, the AGN confirmation, at least from ID10646 and ID3686, suggests an increase of the AGN fraction toward the bright end. Such a trend has been confirmed at $z \sim 2$–7 (e.g., Y. Ono et al. 2018; D. Sobral et al. 2018; R. A. A. Bowler et al. 2021; S. L. Finkelstein & M. B. Bagley 2022). Further comprehensive AGN searches and follow-up observations may unveil even higher AGN fractions at $z \gtrsim 9$ and provide a reasonable answer to the origin of the high abundance of UV-bright galaxy candidates at $z \gtrsim 9$ (Section 4.3).

5. Bubbles in the Shadow at $z = 8.5$

In Section 3.1, we find that the $z_{\rm break}$ measurements are underestimated in ID20466 and ID10646, compared to their $z_{\rm line}$ measurements. This is caused by the nonzero fluxes blueward of the Lyα emission in the prism spectra. Such an enhanced transmission of the Lyα line and continuum is thought to be attributed to the presence of the so-called proximity zone, which has often been observed around high-redshift luminous quasars due to their strong radiation making the surrounding IGM neutral gas fully ionized (e.g., A.-C. Eilers et al. 2017). In addition to the unambiguous AGN feature observed in ID20466 via the broad Hβ line, ID10646 also shows several uniquely high-ionization lines (e.g., N IV] λ1487, C IV λ1549, and He II λ1640), suggesting the presence of an AGN and/or star-forming activities that produce the strong radiation. Furthermore, ID20466 and ID10646 turn out to be the same redshift with a physical distance of 380 kpc in the source plane, where they might reside in the same ionized bubble.

Figure 9 presents the zoom-in 2D + 1D prism spectra of ID10646 and ID20466 with the expected wavelength of the Lyα break based on $z_{\rm line}$ (magenta vertical line). In both spectra, we clearly identify emission blueward of the Lyα break, indicating the presence of ionized bubbles around these systems. Note that NIRSpec meets the requirement of wavelength accuracy of one-eighth of a resolution element (T. Böker et al. 2023), corresponding to ∼0.25 pixels, and thus the uncertainty of the wavelength calibration is not the cause. To evaluate the proximity zone radius $R_{\rm p}$, we model the IGM absorption in the same manner as T. Totani et al. (2006). For the intrinsic rest-frame UV spectrum, we perform a power-law fit at 1.2–2.0 μm, masking the $\pm$0.05 μm range of the bright emission lines detected in the spectrum. We then convolve the best-fit power law with the spectral resolution of NIRSpec/prism, multiply the IGM absorption model, and infer the best-fit $R_{\rm p}$ value from the minimum χ^2 method. Although blueward of the Lyα line is also clearly detected from ID20466, we conduct this measurement only for ID10646, because of the difficulties from (i) the absence of emission blueward of the Lyα continuum in the spectrum, (ii) the uncertainty in modeling the intrinsic SED with its heavily dust-reddened nature, and (iii) the uncertainty in modeling the intrinsic Lyα line profile with the current spectral resolution.

In Figure 9, we show the best-fit IGM absorbed SED for ID10646 (red curve). We obtain the best-fit value of $R_{\rm p} = 7.69 \pm 0.18$ pMpc. To evaluate the potential effect from a weak Lyα line whose flux may spread into a Gaussian on both sides of the Lyα break (G. C. Jones et al. 2024), we also test the fit, including a Gaussian component on the power law. However, the measured $R_{\rm p}$ values consistently remain at $R_{\rm p} > 7$ pMpc with rest-frame Lyα EWs of 10–100 Å. We thus use the best-fit value from the single power-law fit as a fiducial estimate in this paper. In Figure 10, we also illustrate the ionized bubble and relative positions of ID10646 and ID20466 in the source plane. The best-fit $R_{\rm p}$ value exceeds the physical distance between ID20466 and ID10646. This indicates that these two sources reside in the same ionized bubble. Since ID20466 is a BL AGN, the ongoing and/or past quasar active phases in ID20466 might play a key role in contributing to forming the ionized bubble. Yet, we cannot rule out the possibility that ID10646 is the main driver of the formation of this ionized bubble, given the numerous detections of its high-ionization lines. A galaxy overdensity might also be related,

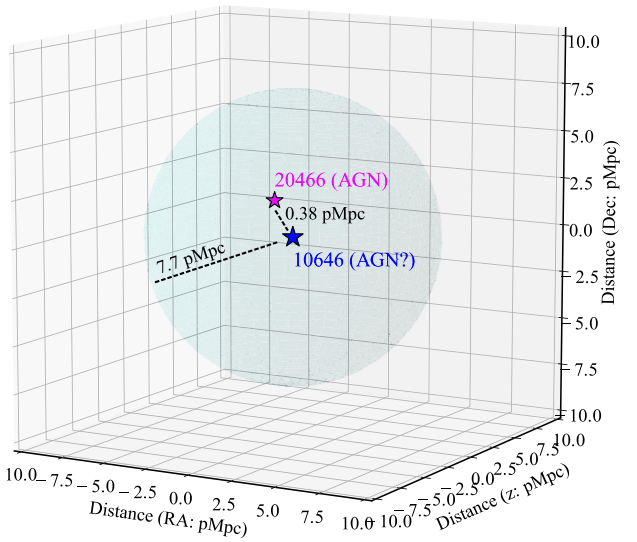

Figure 10. Schematic illustration of the relative 3D positions of ID20466 and ID10646 in the source plane. The source plane coordinates of ID20466 and ID10646 are (R.A., decl.) = (3.63506157, −30.44818861) and (3.63209972, −30.46295758), respectively. The light blue shaded sphere denotes an isotropic sphere of the ionized bubble with $R_p = 7.7$ pMpc measured from the blueward Lyα line and continuum emission in the prism spectrum of ID10646. Their physical distance of 0.38 pMpc indicates that ID20466 also resides in the same ionized bubble, which facilitates the blueward Lyα emission also observed from ID20466, and the AGN activity in ID20466 (and ID10646) may contribute to forming this ionized bubble.

where many faint galaxies contribute to forming the ionized bubble.

In Figure 11, we also compare our R_p measurement with those of luminous quasars at $z \gtrsim 6$ in the literature (A.-C. Eilers et al. 2017; R. Ishimoto et al. 2020). Because ID20466 also resides in the same ionized bubble and might play a key role in its formation, we also show the dust-corrected measurement for ID20466.[35] For comparison, we also present the best-fit R_p−M_{UV} relation for the $z \sim 6$ quasars estimated in R. Ishimoto et al. (2020) and the trend obtained from the radiative transfer simulations presented in A.-C. Eilers et al. (2017). These empirical and theoretical predictions show a positive correlation between M_{UV} and R_p. Remarkably, we find that ID10646 and ID20466 fall in significantly faint M_{UV} and large R_p parameter space, ∼1–2 orders of magnitude fainter M_{UV} than what is predicted from the typical positive correlation obtained both from the previous observational and theoretical results. These remarkable gaps indicate the following three possible interpretations: (i) ID20466 and/or ID10646 had more luminous quasar phases until recently, (ii) the IGM gas density is much lower around these two sources than those of the luminous quasars at $z \sim 6$, which enables them to form a large R_p with a relatively low luminosity,[36] and (iii) there exist many faint galaxies around that are the main drivers of the ionized bubble. If the first interpretation is the case, the correlations of M_{UV} and R_p suggest that the more luminous phase of these objects could reach $M_{UV} \lesssim -26$. From the survey volume in UNCOVER at $z \sim 8.5$, the predicted number of such luminous quasars ($M_{UV} \lesssim -26$) is $\ll 10^{-5}$ (e.g., P. Dayal et al. 2019), indicating that the presence of such a single luminous quasar is already extremely challenging to our current black hole formation and evolution models. In the interpretation of (ii), given that Strömgren radius $\propto n_{gas}^{-2/3}$, a gas density lower than the environment around the luminous quasars by a factor of ∼100 may explain that ID20466 provides a sufficient amount of the ionizing photon budget to form the observed proximity zone. Nevertheless, this interpretation still requires the covering fraction of the dusty cloud around the AGN to be low, where most ionizing photons successfully escape from the system to ionize the surrounding neutral IGM. In the interpretation of (iii), although we do not find evidence of a galaxy overdensity at $z \sim 8.5$ in our SED catalog (B. Wang et al. 2024), these galaxies fall close to the edge of the primary area of the UNCOVER NIRCam observations (Figure 1), which might make it difficult to identify nearby faint galaxies at the same redshift.

Interestingly, we also observe the Lyα line from ID20466, despite its heavily dusty nature with $A_V = 2.1$ (Section 3.1). The giant ionized bubble may facilitate the Lyα line, including the blueward emission, while the heavily dusty nature indicates that the origin of the Lyα line is not the emission of the BL AGN from the line of sight. Instead, there are the following three possible scenarios for the origin of the Lyα line from ID20466: (a) cold gas inflow, (b) a blue, unobscured host galaxy, or (c) scattered light that escaped from angles different from the dust-obscured AGN line of sight.

In the scenario of (a), we include a single Gaussian with the power-law function, convolve with the wavelength-dependent spectral resolution of the prism, and fit it to the prism spectra at 0.9−1.6 μm to measure the velocity offset of the Lyα line peak. We find that the Lyα peak is blueshifted by 2500 ± 300 km s^{-1} (≃0.01 μm) with respect to the systemic redshift determined by other emission lines (z_{line}). However, the velocity scale of the cold gas inflow is regulated by the gravitational potential (e.g., P. Laursen et al. 2019), which would be comparable to the escape velocity of $\sqrt{2GM_h/R_{vir}}$, where M_h and R_{vir} are the halo mass and virial radius, respectively. Assuming a maximum M_h of $\sim 10^{11}$ M_h at $z = 8.5$ from our survey volume (P. Behroozi et al. 2020) and its R_{vir}, the dynamical velocity is estimated to be ∼200 km s^{-1}. While the resonance scattering nature of the Lyα line can increase the velocity offset by a factor of ∼2 (e.g., A. Verhamme et al. 2006), this indicates that the measured blueshifted velocity is still too high to be explained by cold gas inflow. Instead, a degeneracy between velocity and morphology arises if the Lyα emission is spatially extended and the emitting peak position differs from other emission lines within the MSA shutter. Based on the line-spread function for a uniformly illuminated slit and assuming the resolution element for the prism is 2.2 pixels (P. Jakobsen et al. 2022), we estimate this effect to be up to ∼0.016 μm at 1.1 μm if the peak of the Lyα distribution is located on the opposite side of the microshutter compared to the other line-emitting gas. The measured Lyα offset is equal to ∼0.01 μm, indicating that the Lyα offset in the prism may be explained by this differential morphology effect within the shutter, although we do not find any clear evidence of the differential morphology in the F115W that includes the Lyα line emission. To give a definitive answer, we need high spectral resolution follow-up and a detailed Lyα line profile. In the scenario of (b), it might be the case that the AGN core is heavily dust reddened, while the host galaxy is a blue,

[35] We use the bolometric luminosity estimate of $L_{bol} = 6.6 \times 10^{45}$ erg s^{-1} (V. Kokorev et al. 2023) and assume a bolometric luminosity correction factor of 4.5 at 1500 Å (G. T. Richards et al. 2006).
[36] Strömgren radius $\propto L^{1/3} \times n_{gas}^{-2/3}$.

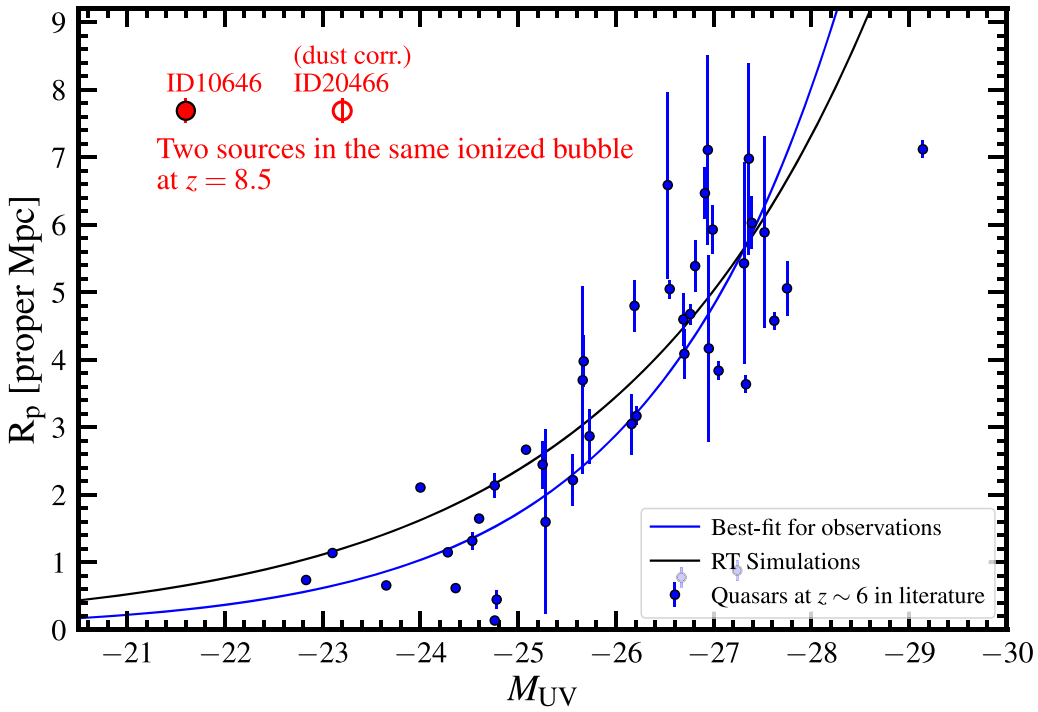

Figure 11. Sizes of the proximity zones (R_p) as a function of M_{UV}. The red filled circle indicates the potential AGN source of ID10646, and the red open circle represents the dusty BL AGN of ID20466 after the dust correction. The blue circles indicate the previous measurements for luminous quasars at $z \sim 6$ (A.-C. Eilers et al. 2018; R. Ishimoto et al. 2020). The blue and black curves are the best-fit relations for the observations (R. Ishimoto et al. 2020) and the radiative transfer simulations (A.-C. Eilers et al. 2017), respectively. ID10646 and ID20466 show remarkable gaps compared to the previous measurements and theoretical trends. In line with the bright Lyα line detection from the dusty BL AGN of ID20466, one interpretation is that the IGM gas density around these two sources is lower than the environment around the luminous quasars at $z \sim 6$ and illuminated by ionizing (and Lyα) photons that escaped from the dusty cloud with a low covering fraction around the AGN. Together with the high AGN abundance from the UV LF measurements at $z \sim 9$–10 (Section 4), the identification of one of the largest ionized bubbles to date around a dusty BL AGN and a possible AGN source indicates the nonnegligible contributions of AGNs to cosmic reionization.

unobscured galaxy from which Lyα is emitted. From the Gaussian and power-law fitting above, we obtain an Lyα luminosity of $\simeq 3.7 \times 10^{42}$ erg s^{-1}. Assuming no dust attenuation and the IGM absorption, we estimate an SFR from this Lyα luminosity of $\simeq 4\ M_\odot$ yr^{-1} using the calibration of R. C. Kennicutt (1998). This SFR value is comparable to a UV luminosity observed at 27.8 mag in F150W, using the R. C. Kennicutt (1998) calibration. However, ID20466 is as faint as 28.8 mag in F150W with a compact morphology, indicating that the emission in F150W is still dominated by an AGN component and that the UV magnitude of the host galaxy is $\gg$28.8 mag. Although there is a scatter between the Hβ/UV luminosity ratio (e.g., C. Simmonds et al. 2023), these properties might indicate that the scenario of (b) is unlikely. In the scenario of (c), the strong Lyα emission is originally from the AGN, and its resonance scattering nature helps to avoid the dusty cloud in the line of sight. It has also been argued that the rest-frame UV light in these red compact objects like ID20466 may be caused by scattered light (e.g., R. J. Assef et al. 2020; E. Glikman et al. 2023; A. Noboriguchi et al. 2023) based on their unique SED shape in the blue (UV) and red (optical) colors (I. Labbe et al. 2023b). In this process, the Lyα may be scattered and thus avoid the dusty clouds, similarly to the rest-frame UV light, while the ionizing photons can escape to the IGM from holes in the neutral hydrogen and may directly contribute to forming the ionized bubble around ID20466. It is worth mentioning that the scattered Lyα line may be an extended, so-called Lyα halo (e.g., F. Leclercq et al. 2020), which is also well aligned with the "blueshifted" Lyα peak observed in ID20466, because the blueshifted Lyα peak is explained by the differential morphology effect within the shutter, as described above.

In short, (c) is the most likely scenario among these three, which is also in line with the interpretation of the remarkable gap observed in the M_{UV}–R_p relation that ID20466 (and ID10646) forms the giant ionized bubble in a relatively low-density IGM environment (interpretation (ii)). Despite the small survey volumes, dozens of dust-reddened compact objects have been identified in recent HST and JWST studies at $z \sim 4$–7 (e.g., S. Fujimoto et al. 2022; R. Endsley et al. 2023; L. J. Furtak et al. 2023a; I. Labbe et al. 2023b), and some have already been spectroscopically confirmed to be AGNs from BL Balmer line detection (D. D. Kocevski et al. 2023; J. Matthee et al. 2024; L. J. Furtak et al. 2024). These identifications indicate a high abundance of dusty AGNs at high redshifts, resulting in steeper faint-end slopes of the AGN LFs at $z \sim 4$–7 (e.g., I. Labbe et al. 2023b; J. Matthee et al. 2024) than what is estimated from previous Type I quasar measurements (e.g., M. Akiyama et al. 2018; Y. Matsuoka et al. 2018; I. D. McGreer et al. 2018). While their dusty nature has implied that their contributions to cosmic reionization are minimal, the discovery of the giant ionized bubble and the bright Lyα line detected from ID20466 suggests its potential contributions to forming the ionized bubble, despite its heavily dusty nature. Importantly, a similarly bright Lyα line is also observed in another dusty BL AGN at $z = 7.0$ ($A_V \sim 3$; L. J. Furtak et al. 2024). If a situation similar to ID20466 is also taking place in other dusty BL AGNs, the ionizing photon escape from dusty AGNs may be a recurrent event at the heart of the epoch of cosmic reionization. While recent spectroscopic

observations for faint galaxies (down to $M_{\rm UV}=-15$) at $z\simeq 6$–8 provide firm evidence that the main driver of cosmic reionization is galaxies (H. Atek et al. 2024), our results imply that the abundant (dusty) AGNs at $z\gtrsim 9$ may still have nonnegligible contributions to cosmic reionization.

6. Summary

In this paper, we present JWST NIRSpec prism follow-up MOS observations using the MSA for $z\gtrsim 9$ galaxy candidates. These candidates were identified in the Cycle 1 Treasury program of UNCOVER (#2561; PIs: I. Labbe and R. Bezanson; R. Bezanson et al. 2024) behind the massive galaxy cluster A2744. Owing to its extensive designs of the NIRSpec observations among the lensing cluster surveys in JWST Cycle 1, these new deep prism spectra, leveraged by the gravitational lensing effect, afford us unparalleled opportunities to perform the initial spectroscopic census of these early galaxies and investigate the UV LF, the AGN fraction, and their contributions to cosmic reionization out to the redshift frontier in a wide UV luminosity range. The major findings of this paper are summarized below.

1. Of the 680 distinct targets in our NIRSpec MSA, we confirm the source redshift via emission lines and/or the Lyα break feature in the prism spectra for 10 lensed galaxies ($\mu=1.3$–12.8) ranging from $z=8.50$ to 13.08. These galaxies have an $M_{\rm UV}$ range of $\in[-21.72, -17.28]$ after lensing corrections. This increases the spec-z-confirmed sample so far known in the high-redshift ($z\gtrsim 9$) and UV-faint ($M_{\rm UV}\gtrsim -19$) regime by a factor of 3.
2. Although the 10 spec-z-confirmed sources are initially selected through several different selection criteria, four sources are in the sample selected from a systematic NIRCam analysis presented in A23, which achieves a high confirmation rate of 100%. Six sources show robust multiple emission-line detections, providing the most secure redshift estimates. The other four sources are mainly constrained with the Lyα break feature.
3. For the homogeneous sample from A23, we do not find systematic overestimates in $z_{\rm phot}$ from $z_{\rm spec}$ reported in recent NIRSpec studies, probably owing to the deep blue NIRCam filters (F115W and F150W) taken in UNCOVER and some strict selection criteria adopted in the A23 selection. Using six sources with multiple emission-line detection, we also evaluate the offset of the redshift estimates between the lines ($z_{\rm line}$) and the Lyα break ($z_{\rm break}$). We find that the offset can be as large as out to ± 0.2. This offset can be even worse with lower SNR data, which raises caution in designing future follow-up spectroscopy for the break-only sources, especially with ALMA.
4. In addition to the X-ray-luminous AGN confirmed at $z=10.07$ (A. D. Goulding et al. 2023), we newly identify a dusty BL AGN at $z=8.50$ (V. Kokorev et al. 2023). Besides, the prism spectra for the two most UV-luminous galaxies in our spec-z sample hint at AGN activity. This is inferred from several highly ionized gas emission lines detected at high significance levels (e.g., N IV] λ1487, C IV λ1549, and He II λ1640) and an elevated [O III] $\lambda5008/{\rm H}\beta$ ratio exceeding 10 observed in ID10646 and ID3686.
5. In conjunction with the spec-z-confirmed sources in UNCOVER and other general field surveys of CEERS and JADES, we infer lower bounds on the UV LFs at $z\sim 9$, $z\sim 10$, and $z\sim 12$. Our results align with previous photometric measurements and improve the lower constraints previously established from recent spectroscopic studies. Our results also confirm the high abundance of the UV-bright ($M_{\rm UV}\lesssim -20$) galaxies at $z\gtrsim 9$, which challenges several current theoretical models. In the $z\sim 9$ UV LF, we find a significant excess in the brightest $M_{\rm UV}$ bin, spanning $[-22, -21]$, comprising ID10646 and ID3686. Given their different redshifts, this excess is attributable not to an overdensity but to their uniquely UV-bright properties. This further reinforces the hypothesis that these UV-luminous sources, characterized by multiple high-ionization emission lines, are indeed AGNs.
6. With the spec-z-confirmed BL AGN and X-ray-luminous AGN, we also evaluate the lower limits on the AGN LFs at $z\sim 9$ and $z\sim 10$. These lower limits require the AGN LFs at $z\sim 9$–10 to have a comparable or even higher amplitude than the X-ray AGN LF estimated at $z\sim 6$.
7. Our results suggest a relatively high AGN fraction of $>10\%$–35% even at $z\gtrsim 9$, compared to the previous reports of $\approx 5\%$–10% from BL AGN identifications at $z\sim 4$–7. This high AGN fraction is likely attributed to the comprehensive AGN recognition made feasible by our intensive 2.7–11.8 hr prism exposures (see $\sim$1–2.6 hr in previous NIRSpec studies for BL AGN searches) and the ancillary deep X-ray data, both of which benefit substantially from the gravitational lensing effect. These results indicate the plausible cause of the high abundance of $z>9$ galaxies claimed in the recent photometric studies may be the AGNs.
8. We identify nonzero fluxes blueward of the Lyα emission in the prism spectra of the dusty BL AGN of ID20466 at $z=8.50$ and the potential AGN source of ID10646 at $z=8.51$. The proximity zone size measurement shows that these two sources resided in the same ionized bubble with $R_{\rm p}=7.69\pm 0.18$ pMpc. Both these sources notably deviate from the established $M_{\rm UV}$–$R_{\rm p}$ relationship observed in luminous quasars at $z\sim 6$. Despite its heavily dusty nature with $A_V=2.1$, the Lyα line is also detected from ID20466. A plausible explanation is that the covering fraction of the dusty cloud surrounding the AGN is minimal, thereby facilitating significant ionizing photon escape. This is in line with our identification of the giant ionized bubble. Our results, taken in concert with indications of the high AGN fraction even at $z\gtrsim 9$, suggest that AGNs might have played a nonnegligible role during cosmic reionization.

Acknowledgments

We thank the anonymous referee for the helpful and constructive review on the paper. We also thank Peter Larson, Darach Watson, Charlotte Mason, Kohei Inayoshi, and Akio Inoue for helpful discussions on the proximity zone size measurements and the interpretation of the ionized bubble identified at $z=8.5$. We are also grateful to Steven Finkelstein and Pablo Arrabal-Haro for valuable discussions and for sharing the materials for the survey volume calculations for the NIRSpec

programs conducted in the CEERS field. We also thank Rohan Naidu for discussing the spec-z confirmation results for $z > 10$ galaxies, Nikko Cleri for discussing the UV emission-line properties, and Maximilien Franco for sharing the UV LF measurements. This work is based on observations made with the NASA/ESA/CSA James Webb Space Telescope. The data were obtained from the Mikulski Archive for Space Telescopes at the Space Telescope Science Institute, operated by the Association of Universities for Research in Astronomy, Inc., under NASA contract NAS5-03127 for JWST. These observations are associated with program JWST-GO-2561. Support for program JWST-GO-2561 was provided by NASA through a grant from the Space Telescope Science Institute, which is operated by the Association of Universities for Research in Astronomy, Inc., under NASA contract NAS 5-03127. This project has received funding from NASA through the NASA Hubble Fellowship grant HST-HF2-51505.001-A awarded by the Space Telescope Science Institute, which is operated by the Association of Universities for Research in Astronomy, Incorporated, under NASA contract NAS5-26555. H.A. and I. C. acknowledge support from CNES, focused on the JWST mission, and the Program National Cosmology and Galaxies (PNCG) of CNRS/INSU with INP and IN2P3, cofunded by CEA and CNES. P.D. acknowledges support from the NWO grant 016.VIDI.189.162 ("ODIN") and from the European Commission's and University of Groningen's CO-FUND Rosalind Franklin program. A.Z. and L.J.F. acknowledge support by grant No. 2020750 from the United States-Israel Binational Science Foundation (BSF) and grant No. 2109066 from the United States National Science Foundation (NSF), and by the Ministry of Science & Technology, Israel. This work has received funding from the Swiss State Secretariat for Education, Research and Innovation (SERI) under contract number MB22.00072, as well as from the Swiss National Science Foundation (SNSF) through project grant 200020_207349. The Cosmic Dawn Center (DAWN) is funded by the Danish National Research Foundation under grant No. 140. The work of C.C.W. is supported by NOIRLab, which is managed by the Association of Universities for Research in Astronomy (AURA) under a cooperative agreement with the National Science Foundation. M.S. acknowledges support from the CIDEGENT/2021/059 grant, from project PID2019-109592GB-I00/AEI/10.13039/501100011033 from the Spanish Ministerio de Ciencia e Innovación—Agencia Estatal de Investigación. M. S.T. also acknowledges the financial support from the MCIN with funding from the European Union NextGenerationEU and Generalitat Valenciana in the call Programa de Planes Complementarios de I + D + i (PRTR 2022) Project (VALJPAS), reference ASFAE/2022/025.

Some/all of the data presented in this paper were obtained from the Mikulski Archive for Space Telescopes (MAST) at the Space Telescope Science Institute. The specific observations analyzed can be accessed via doi:10.17909/bvf5-mp20. The reduced data is also available via https://jwst-uncover.github.io/.

Software: `msaexp` (0.6.10; G. Brammer 2022), `astropy` (Astropy Collaboration et al. 2013, 2018, 2022), `eazy` (G. B. Brammer et al. 2008), `FSPS` (C. Conroy & J. E. Gunn 2010), and Prospector (B. D. Johnson et al. 2021).

Appendix A
Details of Individual Sources

Below, we briefly summarize the information for the 10 spec-z-confirmed UNCOVER sources presented in this paper.

20466 ($z = 8.50$). This source is included in the MSA as a high-redshift dusty AGN candidate due to the red color and compact morphology (ID13556 in I. Labbe et al. 2023b). We observed this source once in MSA-2 with an exposure time of 2.7 hr. In addition to the Lyα break feature, multiple emission lines are detected at SNR $\geqslant 2.5$, such as Lyα, Mg II $\lambda\lambda$ 2796, 2803, [Ne III] λ3869, [Ne III] λ3968, [O III] λ4363, [O III] λ4960, [O III] λ5008, Hδ, Hγ, and Hβ, constraining its redshift at $z = 8.500^{+0.000}_{-0.001}$. The unambiguous BL emission is identified in Hβ, being the highest-redshift BL AGN whose BL Balmer line is securely (SNR > 5) detected so far (see also R. L. Larson et al. 2023). The Lyα line, bluer than its rest-frame 1216 Å, is also detected, and we discuss its possible physical origins in Section 5. The photometric catalog ID is 21347 (J. R. Weaver et al. 2024). Further details of the sample selection and characterizations will be presented in J. Greene et al. (2024, in preparation) and V. Kokorev et al. (2023).

10646 ($z = 8.51$). This source is included in the MSA due to its uniquely red color (F277W – F444W = 1.2 mag). We observed this source once in MSA-2 with an exposure time of 2.7 hr. In addition to the unambiguous Lyα break, multiple emission lines are detected at SNR $\geqslant 2.5$, such as N IV] λ1487, C IV λ1549, O III] $\lambda\lambda$1661, 1666, He II λ1640, C III] $\lambda\lambda$1907, 1909, Mg II $\lambda\lambda$ 2796, 2803, [Ne V] λ3346, [O II] $\lambda\lambda$3727, 3730, [Ne III] λ3869, [Ne III] λ3968, [O III] λ4363, [O III] λ4960, [O III] λ5008, Hγ, Hδ, Hβ, and He I, constraining its redshift at $8.511^{+0.000}_{-0.001}$. Note that the [Ne V] λ3426/[Ne V] λ3346 ratio is almost constant at 2.73. We confirm [Ne V] λ3426 is also observed in our spectrum with SNR ~ 2, while it indicates [Ne V] λ3426/[Ne V] λ3346 ~ 1. This might suggest that the [Ne V] λ3346 line detection could be spurious, although it is challenging to conclude with their current SNRs. ID10646 is spatially separated from ID20466 by a physical scale of 380 kpc in the source plane, and their redshift difference is only 0.01. We thus interpret these sources as residing in the same massive dark matter halo. Similar to ID20466, the continuum blueward of the Lyα line is also detected in ID10646, and we discuss its possible physical origins in Section 5. ID10646 is uniquely UV bright. With $M_{\rm UV} = -21.5$ mag, it is comparably bright to GNz11 (e.g., A. J. Bunker et al. 2023) and shows several highly ionized gas emission lines at high significance levels (e.g., N IV] λ1487, C IV λ1549, and He II λ1640). However, we cannot rule out the possibility that the galaxy emission is driven by star-forming activity rather than an AGN based on rest-frame UV–optical line diagnostics alone (e.g., A. Feltre et al. 2016). The photometric catalog ID is 11701 (J. R. Weaver et al. 2024). Further details and characterizations will be presented in J. Weaver et al. (2024, in preparation).

3686 ($z = 9.33$). This source is included in the MSA as one of the robust $z > 9$ candidates selected in A23. We observed this source once in MSA-2 with an exposure time of 2.7 hr. In addition to the unambiguous Lyα break, multiple emission lines are detected at SNR $\geqslant 2.5$, such as N IV] λ1487, [Ne V] λ3426, [O II] $\lambda\lambda$3723, 3730, [Ne III] λ3869, [O III] λ4960, [O III] λ5008, and Hγ, constraining its redshift at $z = 9.325^{+0.000}_{-0.001}$. As part of the GLASS-JWST survey

(#1324; PI: T. Treu; T. Treu et al. 2022) and a follow-up DDT program (#2756; PI: W. Chen), a consistent NIRSpec/prism spectroscopic confirmation has also been reported in K. Boyett et al. (2024), while the previous prism observations only cover the wavelength range of ∼1.1–4.5 μm with detector gaps. The full prism spectrum coverage of ∼0.6–5.2 μm newly detects several emission lines from this source, including N IV] λ1487, Hβ and [O III] λ4960, 5008. On the other hand, the [Ne V] λ3426 line is not detected in the previous observations, although its observed wavelength was covered by the previous observations. This suggests that the [Ne V] λ3426 line could be spurious, while the shutter configurations of MSA are not exactly the same between previous and our observations. The source is spatially extended, indicative of an interacting system (K. Boyett et al. 2024). ID3686 is the most luminous high-redshift galaxy candidate at $z \gtrsim 9$ in the original photometric catalog with $M_{\rm UV} = -21.7$. Employing a nearby empty shutter, we also produce spectra for the three shutters with the global background subtraction, where the [O III] λ5008/Hβ shows uniquely high ratios of ∼11–18 in the central and southeast shutters (see Section 3.1). These ratios exceed the maximum value of ∼10 observed in recent NIRSpec studies for galaxies at $z \sim$ 2–9 and fall in the AGN regime in the [N II], [S II], and [O I] BPT diagrams (R. L. Sanders et al. 2023). Such a high ratio may also be induced by shock excitation (e.g., L. J. Kewley et al. 2013; M. Hirschmann et al. 2023), while the fact that a similarly high ratio also observed in the southeast shutter, where the emission is dominated by the compact component in the NIRCam map, indicates that these line properties may be caused by a strong radiation of an AGN. The photometric catalog ID is 4745 (J. R. Weaver et al. 2024).

22223 ($z = 9.57$). This source is included in the MSA as one of $z > 9$ candidates selected from the SED analysis using `eazy` and `prospector` (B. Wang et al. 2024). We observed this source once in MSA-4 with an exposure time of 4.4 hr. In addition to the unambiguous Lyα break, multiple emission lines are detected at SNR $\geqslant$ 2.5, including C IV λ1549, [O III] λ4960, [O III] λ5008, Hδ, Hγ, and Hβ. In the 2D spectrum, we also identify an unknown line at ∼0.9 μm, probably due to a failed open shutter, though our extraction does not include either positive or negative features from this line, and thus this does not affect our results. The prism spectrum shows a softened Lyα break shape, also reported in other $z > 9$ prism-observed galaxies. This shape is likely caused by some combination of effects of the Lyα damping wing, the intrinsic SED shape, and/or an additional DLA system (e.g., P. Arrabal Haro et al. 2023b; E. Curtis-Lake et al. 2023; K. E. Heintz et al. 2024; H. Umeda et al. 2024). The photometric catalog ID is 23089 (J. R. Weaver et al. 2024).

31028 ($z = 9.74$). This source is included in the MSA as one of $z > 9$ candidates with a high magnification ($\mu > 5$) selected from SED analysis using `eazy` and `prospector` (B. Wang et al. 2024). We observe this source in MSA-3 and MSA-6, with a total exposure time of 6.9 hr. However, due to the lack of an obvious continuum trace in the 2D spectrum taken in MSA-3, probably because of more significant slit loss (see Figure 2) and the potential systematic uncertainty in the slit-loss correction in the coadd process, we only use the data taken in MSA-6 in this paper (4.4 hr). Our template fitting supports the high-z solution from the Lyα break feature (see also the blue curve representing the forced low-z best-fit solution in Figure 3), constraining its redshift at $z = 9.740^{+0.000}_{-0.001}$, where the Ly$\alpha$ line is tentatively detected at SNR ∼ 3. No emission lines are detected above SNR $\geqslant$ 2.5. The redshift estimate subsequently leads to a magnification estimate of $\mu = 6.73^{+1.50}_{-0.05}$ and $M_{\rm UV} = -17.31$ mag, making it intrinsically the faintest source among the spec-z-confirmed objects at $z \geqslant 8.5$ with JWST so far (e.g., P. Arrabal Haro et al. 2023a, 2023b; S. Fujimoto et al. 2023c; G. Roberts-Borsani et al. 2023; H. Williams et al. 2023; K. N. Hainline et al. 2024). The photometric catalog ID is 31955 (J. R. Weaver et al. 2024).

13151 ($z = 9.88$). This source is included in the MSA as one of $z > 9$ candidates with a high magnification ($\mu > 5$) selected from the SED analysis using `eazy` and `prospector` (B. Wang et al. 2024). We observed this source three times in MSA-5, MSA-6, and MSA-7, with a total exposure time of 11.8 hr. In addition to the unambiguous Lyα break, multiple emission lines are detected at SNR $\geqslant$ 2.5, including O III] $\lambda\lambda$1661, 1666 and C III] $\lambda\lambda$1907, 1909. Previous NIRSpec/prism observations detect the Lyα break feature, providing a redshift solution of $z = 9.79$ via a similar `eazy` template fitting method (G. Roberts-Borsani et al. 2023), while the multiple emission-line identification and the better sensitivity in the Lyα break make the redshift solution firmly improved. The photometric catalog ID is 14088 (J. R. Weaver et al. 2024).

26185 ($z = 10.07$). This source is included in the MSA as one of the robust $z > 9$ candidates selected in A23 (see also, e.g., M. Castellano et al. 2023). Moreover, an X-ray-luminous AGN has been reported from a 1.25 Ms deep Chandra observation, making this the highest-z X-ray AGN known (A. Bogdan et al. 2024). We observe this source twice in MSA-1 and MSA-4, with a total exposure time of 7.1 hr. In addition to the unambiguous Lyα break, multiple emission lines are detected at SNR $\geqslant$ 2.5, such as C III] $\lambda\lambda$1709, 1909, [O II] $\lambda\lambda$3727, 3730, [Ne III] λ3869, [Ne III] λ3968, and Hγ, constraining its redshift at $z = 10.071^{+0.000}_{-0.001}$. The photometric catalog ID is 27025 (J. R. Weaver et al. 2024). Further details and characterizations have been presented in A. D. Goulding et al. (2023) as UHZ1.

37126 ($z = 10.23$). This source is included in the MSA as one of the robust $z > 9$ candidates selected in A23. We observed this source twice in MSA-3 and MSA-4, with a total exposure time of 6.9 hr. The source failed to be successfully extracted from MSA-3 in our early reduction, and thus we use the data from MSA-4 (4.4 hr) in this analysis. The peaky feature at ∼4.8 μm in the spectrum is an artifact, and we mask the relevant pixels in our template fitting. From the unambiguous Lyα break, the redshift is securely estimated at $z = 10.255^{+0.001}_{-0.001}$ with N III] $\lambda\lambda$ 1747, 1749 detection at SNR ∼ 3. The photometric catalog ID is 38095 (J. R. Weaver et al. 2024).

38766 ($z = 12.39$). This source is included in the MSA as one of the robust $z > 12$ candidates selected in A23. We observed this source once in MSA-4, with an exposure time of 4.4 hr. The unambiguous Lyα break and a tentative He I line (SNR ∼ 2.5) are detected, constraining the source redshift at $z = 12.393^{+0.004}_{-0.001}$. At a consistent redshift, tentative [O II] $\lambda\lambda$3727, 3730 and Mg II $\lambda\lambda$ 2796,2803 are also detected (SNR ∼ 2). Within ∼2′ on the sky, a remarkably UV-bright galaxy is identified with a very close photometric redshift ($z_{\rm phot} = 12.4^{+0.1}_{-0.3}$; R. P. Naidu et al. 2022b; see also M. Castellano et al. 2022; R. Bouwens et al. 2023a; C. T. Donnan et al. 2023; Y. Harikane et al. 2023a), where there might exist a galaxy overdensity. The photometric catalog ID is 39753

(J. R. Weaver et al. 2024). Further details and characterizations have been presented in B. Wang et al. (2023a) as UNCOVER-z12.

13077 ($z = 13.08$). This source is included in the MSA as one of $z > 12$ candidates selected from the SED analysis using `eazy` and `prospector` (B. Wang et al. 2024). We observe this source twice in MSA-5 and MSA-7, with a total exposure time of 7.4 hr. No emission lines are detected above SNR $\geqslant 2.5$, while our template fitting shows the high-z solution from the Lyα break feature (see also the blue curve representing the forced low-z best-fit solution in Figure 3), constraining its redshift at $z = 13.079^{+0.014}_{-0.001}$. Although the Ly$\alpha$ break feature is less secure than other sources, the template fittings to both individual spectra taken in MSA-5 and MSA-7 show the high-z solution as well. The photometric catalog ID is 14019 (J. R. Weaver et al. 2024). Further details and characterizations have been presented in B. Wang et al. (2023a) as UNCOVER-z13.

Appendix B
IDs in Different Literature

Our 10 spec-z-confirmed sources have also been reported in previous studies in various contexts. In Table 4, we summarize the IDs of the 10 spec-z-confirmed sources presented in different literature.

Table 4
IDs of the 10 Spec-z-confirmed Sources at $z \geqslant 8.5$ in Our UNCOVER/NIRSpec Observations

ID (This) (1)	ID (Wa23) (2)	ID (Other) (3)
20466	21347	13556 (L23)
10646	11701	⋯
3686	4745	Gz9p3 (B23), 2065 (A23), DHZ1 (C23)
22223	23089	⋯
31028	31955	⋯
13151	14088	JD1 (Z14), (RB23)
26185	27025	UHZ1 (C23), 21623 (A23)
37126	38095	39704 (A23)
38766	39753	42329 (A23), UNCOVER-z12 (Wa23)
13077	14019	UNCOVER-z13 (Wa23)

Note. (1) Source ID used in the MSA design and this paper. (2) Source ID used in the UNCOVER photometric catalog of J. R. Weaver et al. (2024). (3) Source ID or name used in other literature (L23: I. Labbe et al. 2023b; A23: H. Atek et al. 2023b; B23: K. Boyett et al. 2024; C23: M. Castellano et al. 2023; RB23: G. Roberts-Borsani et al. 2023; G23: A. D. Goulding et al. 2023; Wa23: B. Wang et al. 2023a; and Z14: A. Zitrin et al. 2014).

ORCID iDs

Seiji Fujimoto https://orcid.org/0000-0001-7201-5066
Bingjie Wang https://orcid.org/0000-0001-9269-5046
John R. Weaver https://orcid.org/0000-0003-1614-196X
Vasily Kokorev https://orcid.org/0000-0002-5588-9156
Hakim Atek https://orcid.org/0000-0002-7570-0824
Rachel Bezanson https://orcid.org/0000-0001-5063-8254
Ivo Labbe https://orcid.org/0000-0002-2057-5376
Gabriel Brammer https://orcid.org/0000-0003-2680-005X
Jenny E. Greene https://orcid.org/0000-0002-5612-3427
Iryna Chemerynska https://orcid.org/0009-0009-9795-6167
Pratika Dayal https://orcid.org/0000-0001-8460-1564
Anna de Graaff https://orcid.org/0000-0002-2380-9801
Lukas J. Furtak https://orcid.org/0000-0001-6278-032X
Pascal A. Oesch https://orcid.org/0000-0001-5851-6649
David J. Setton https://orcid.org/0000-0003-4075-7393
Sedona H. Price https://orcid.org/0000-0002-0108-4176
Tim B. Miller https://orcid.org/0000-0001-8367-6265
Christina C. Williams https://orcid.org/0000-0003-2919-7495
Katherine E. Whitaker https://orcid.org/0000-0001-7160-3632
Adi Zitrin https://orcid.org/0000-0002-0350-4488
Sam E. Cutler https://orcid.org/0000-0002-7031-2865
Joel Leja https://orcid.org/0000-0001-6755-1315
Richard Pan https://orcid.org/0000-0002-9651-5716
Dan Coe https://orcid.org/0000-0001-7410-7669
Pieter van Dokkum https://orcid.org/0000-0002-8282-9888
Robert Feldmann https://orcid.org/0000-0002-1109-1919
Yoshinobu Fudamoto https://orcid.org/0000-0001-7440-8832
Andy D. Goulding https://orcid.org/0000-0003-4700-663X
Gourav Khullar https://orcid.org/0000-0002-3475-7648
Danilo Marchesini https://orcid.org/0000-0001-9002-3502
Michael Maseda https://orcid.org/0000-0003-0695-4414
Themiya Nanayakkara https://orcid.org/0000-0003-2804-0648
Erica J. Nelson https://orcid.org/0000-0002-7524-374X
Renske Smit https://orcid.org/0000-0001-8034-7802
Mauro Stefanon https://orcid.org/0000-0001-7768-5309
Andrea Weibel https://orcid.org/0000-0001-8928-4465

References

Adams, N. J., Conselice, C. J., Ferreira, L., et al. 2023, MNRAS, 518, 4755
Akiyama, M., He, W., Ikeda, H., et al. 2018, PASJ, 70, S34
Andika, I. T., Jahnke, K., Onoue, M., et al. 2020, ApJ, 903, 34
Arrabal Haro, P., Dickinson, M., Finkelstein, S. L., et al. 2023a, Natur, 622, 707
Arrabal Haro, P., Dickinson, M., Finkelstein, S. L., et al. 2023b, ApJL, 951, L22
Assef, R. J., Brightman, M., Walton, D. J., et al. 2020, ApJ, 897, 112
Astropy Collaboration, Price-Whelan, A. M., Lim, P. L., et al. 2022, ApJ, 935, 167
Astropy Collaboration, Price-Whelan, A. M., Sipőcz, B. M., et al. 2018, AJ, 156, 123
Astropy Collaboration, Robitaille, T. P., Tollerud, E. J., et al. 2013, A&A, 558, A33
Atek, H., Chemerynska, I., Wang, B., et al. 2023b, MNRAS, 524, 5486
Atek, H., Labbé, I., Furtak, L. J., et al. 2024, Natur, 626, 975
Atek, H., Shuntov, M., Furtak, L. J., et al. 2023a, MNRAS, 519, 1201
Austin, D., Adams, N., Conselice, C. J., et al. 2023, ApJL, 952, L7
Bagley, M. B., Finkelstein, S. L., Rojas-Ruiz, S., et al. 2024, ApJ, 961, 209
Baskin, A., & Laor, A. 2005, MNRAS, 358, 1043
Behroozi, P., Wechsler, R. H., Hearin, A. P., & Conroy, C. 2019, MNRAS, 488, 3143
Behroozi, P., Conroy, C., Wechsler, R. H., et al. 2020, MNRAS, 499, 5702
Behroozi, P. S., & Silk, J. 2015, ApJ, 799, 32
Beichman, C. A., Rieke, M., Eisenstein, D., et al. 2012, Proc. SPIE, 8442, 84422N
Bezanson, R., Labbe, I., Whitaker, K. E., et al. 2024, ApJ, 974, 92
Bhatawdekar, R., Conselice, C. J., Margalef-Bentabol, B., & Duncan, K. 2019, MNRAS, 486, 3805
Bogdan, A., Goulding, A., Natarajan, P., et al. 2024, NatAs, 8, 126
Böker, T., Beck, T. L., Birkmann, S. M., et al. 2023, PASP, 135, 038001
Bouwens, R., Illingworth, G., Oesch, P., et al. 2023a, MNRAS, 523, 1009
Bouwens, R. J., Illingworth, G. D., Oesch, P. A., et al. 2015, ApJ, 803, 34
Bouwens, R. J., Smit, R., Schouws, S., et al. 2022, ApJ, 931, 160
Bouwens, R. J., Stefanon, M., Brammer, G., et al. 2023b, MNRAS, 523, 1036
Bowler, R. A. A., Adams, N. J., Jarvis, M. J., & Häußler, B. 2021, MNRAS, 502, 662
Bowler, R. A. A., Jarvis, M. J., Dunlop, J. S., et al. 2020, MNRAS, 493, 2059
Boyett, K., Trenti, M., Leethochawalit, N., et al. 2024, NatAs, 8, 657
Boylan-Kolchin, M. 2023, NatAs, 7, 731
Bradley, L. D., Coe, D., Brammer, G., et al. 2023, ApJ, 955, 13

Brammer, G., 2022 gbrammer/msaexp: Full Working version with 2D Drizzling and Extraction, v0.3, Zenodo, doi:10.5281/zenodo.7299501
Brammer, G. B., van Dokkum, P. G., & Coppi, P. 2008, ApJ, 686, 1503
Bunker, A. J., Cameron, A. J., Curtis-Lake, E., et al. 2024, A&A, 690, A288
Bunker, A. J., Saxena, A., Cameron, A. J., et al. 2023, A&A, 677, A88
Carnall, A. C., Begley, R., McLeod, D. J., et al. 2023, MNRAS, 518, L45
Castellano, M., Fontana, A., Treu, T., et al. 2022, ApJL, 938, L15
Castellano, M., Fontana, A., Treu, T., et al. 2023, ApJL, 948, L14
Chemerynska, I., Atek, H., Furtak, L. J., et al. 2024, MNRAS, 531, 2615
Conroy, C., & Gunn, J. E. 2010, ApJ, 712, 833
Curtis-Lake, E., Carniani, S., Cameron, A., et al. 2023, NatAs, 7, 622
Dave, R., Angles-Alcazar, D., Narayanan, D., et al. 2019, MNRAS, 486, 2827
Dayal, P., Choudhury, T. R., Bromm, V., & Pacucci, F. 2017, ApJ, 836, 16
Dayal, P., & Ferrara, A. 2018, PhR, 780, 1
Dayal, P., Ferrara, A., Dunlop, J. S., & Pacucci, F. 2014, MNRAS, 445, 2545
Dayal, P., Rossi, E. M., Shiralilou, B., et al. 2019, MNRAS, 486, 2336
Donnan, C. T., McLeod, D. J., Dunlop, J. S., et al. 2023, MNRAS, 518, 6011
Dopita, M. A., & Sutherland, R. S. 1995, ApJ, 455, 468
Eilers, A.-C., Davies, F. B., Hennawi, J. F., et al. 2017, ApJ, 840, 24
Eilers, A.-C., Hennawi, J. F., & Davies, F. B. 2018, ApJ, 867, 30
Ellis, R. S., McLure, R. J., Dunlop, J. S., et al. 2013, ApJL, 763, L7
Endsley, R., Stark, D. P., Lyu, J., et al. 2023, MNRAS, 520, 4609
Feltre, A., Charlot, S., & Gutkin, J. 2016, MNRAS, 456, 3354
Ferrara, A., Pallottini, A., & Dayal, P. 2023, MNRAS, 522, 3986
Finkelstein, S. L., & Bagley, M. B. 2022, ApJ, 938, 25
Finkelstein, S. L., Bagley, M., Song, M., et al. 2022a, ApJ, 928, 52
Finkelstein, S. L., Bagley, M. B., Ferguson, H. C., et al. 2023, ApJL, 946, L13
Finkelstein, S. L., Bagley, M. B., Haro, P. A., et al. 2022b, ApJL, 940, L55
Finkelstein, S. L., Ryan, R. E. J., Papovich, C., et al. 2015, ApJ, 810, 71
Franco, M., Akins, H. B., Casey, C. M., et al. 2024, ApJ, 973, 23
Fujimoto, S., Arrabal Haro, P., Dickinson, M., et al. 2023a, ApJL, 949, L25
Fujimoto, S., Brammer, G. B., Watson, D., et al. 2022, Natur, 604, 261
Fujimoto, S., Finkelstein, S. L., Burgarella, D., et al. 2023b, ApJ, 955, 130
Fujimoto, S., Haro, P. A., Dickinson, M., et al. 2023c, ApJL, 949, L25
Furtak, L. J., Labbé, I., Zitrin, A., et al. 2024, Natur, 628, 57
Furtak, L. J., Zitrin, A., Plat, A., et al. 2023a, ApJ, 952, 142
Furtak, L. J., Zitrin, A., Weaver, J. R., et al. 2023b, MNRAS, 523, 4568
Gardner, J. P., Mather, J. C., Abbott, R., et al. 2023, PASP, 135, 068001
Gehrels, N. 1986, ApJ, 303, 336
Giallongo, E., Grazian, A., Fiore, F., et al. 2019, ApJ, 884, 19
Glikman, E., Rusu, C. E., Chen, G. C. F., et al. 2023, ApJ, 943, 25
Goulding, A. D., Greene, J. E., Setton, D. J., et al. 2023, ApJL, 955, L24
Hainline, K. N., Johnson, B. D., Robertson, B., et al. 2024, ApJ, 964, 71
Harikane, Y., Nakajima, K., Ouchi, M., et al. 2024, ApJ, 960, 56
Harikane, Y., Ouchi, M., Oguri, M., et al. 2023a, ApJS, 265, 5
Harikane, Y., Zhang, Y., Nakajima, K., et al. 2023b, ApJ, 959, 39
Heintz, K. E., Watson, D., Brammer, G., et al. 2024, Sci, 384, 890
Hinshaw, G., Larson, D., Komatsu, E., et al. 2013, ApJS, 208, 19
Hirschmann, M., Charlot, S., Feltre, A., et al. 2019, MNRAS, 487, 333
Hirschmann, M., Charlot, S., Feltre, A., et al. 2023, MNRAS, 526, 3610
Hsiao, T. Y.-Y., Abdurro'uf, Coe, D., et al. 2024, ApJ, 973, 8
Inayoshi, K., Harikane, Y., Inoue, A. K., Li, W., & Ho, L. C. 2022, ApJL, 938, L10
Inayoshi, K., Visbal, E., & Haiman, Z. 2020, ARA&A, 58, 27
Ishimoto, R., Kashikawa, N., Onoue, M., et al. 2020, ApJ, 903, 60
Jakobsen, P., Ferruit, P., Alves de Oliveira, C., et al. 2022, A&A, 661, A80
Johnson, B. D., Leja, J., Conroy, C., & Speagle, J. S. 2021, ApJS, 254, 22
Jones, G. C., Bunker, A. J., Saxena, A., et al. 2024, A&A, 683, A238
Juneau, S., Bournaud, F., Charlot, S., et al. 2014, ApJ, 788, 88
Kannan, R., Springel, V., Hernquist, L., et al. 2023, MNRAS, 524, 2594
Kennicutt, R. C., Jr 1998, ARA&A, 36, 189
Kewley, L. J., Maier, C., Yabe, K., et al. 2013, ApJL, 774, L10
Killi, M., Watson, D., Brammer, G., et al. 2024, A&A, 691, A52
Kocevski, D. D., Onoue, M., Inayoshi, K., et al. 2023, ApJL, 954, L4
Kokorev, V., Fujimoto, S., Labbe, I., et al. 2023, ApJL, 957, L7
Labbe, I., Greene, J. E., Bezanson, R., et al. 2023b, arXiv:2306.07320
Labbe, I., van Dokkum, P., Nelson, E., et al. 2023a, Natur, 616, 266
Larson, R. L., Finkelstein, S. L., Hutchison, T. A., et al. 2022, ApJ, 930, 104
Larson, R. L., Finkelstein, S. L., Kocevski, D. D., et al. 2023, ApJL, 953, L29
Laursen, P., Sommer-Larsen, J., Milvang-Jensen, B., Fynbo, J. P. U., & Razoumov, A. O. 2019, A&A, 627, A84
Leclercq, F., Bacon, R., Verhamme, A., et al. 2020, A&A, 635, A82
Leethochawalit, N., Roberts-Borsani, G., Morishita, T., Trenti, M., & Treu, T. 2023, MNRAS, 524, 5454
Leung, G. C. K., Bagley, M. B., Finkelstein, S. L., et al. 2023, ApJL, 954, L46
Lotz, J. M., Koekemoer, A., Coe, D., et al. 2017, ApJ, 837, 97
Lovell, C. C., Harrison, I., Harikane, Y., Tacchella, S., & Wilkins, S. M. 2023, MNRAS, 518, 2511
Maiolino, R., Scholtz, J., Curtis-Lake, E., et al. 2024a, A&A, 691, A145
Maiolino, R., Scholtz, J., Witstok, J., et al. 2024c, Natur, 627, 59
Maiolino, R., Übler, H., Perna, M., et al. 2024b, A&A, 687, A67
Mason, C. A., Trenti, M., & Treu, T. 2023, MNRAS, 521, 497
Matsuoka, Y., Strauss, M. A., Kashikawa, N., et al. 2018, ApJ, 869, 150
Matthee, J., Naidu, R. P., Brammer, G., et al. 2024, ApJ, 963, 129
Mauerhofer, V., & Dayal, P. 2023, MNRAS, 526, 2196
McGreer, I. D., Fan, X., Jiang, L., & Cai, Z. 2018, AJ, 155, 131
McKinney, J., Finnerty, L., Casey, C. M., et al. 2023, ApJL, 946, L39
McLeod, D. J., McLure, R. J., & Dunlop, J. S. 2016, MNRAS, 459, 3812
Menci, N., Castellano, M., Santini, P., et al. 2022, ApJL, 938, L5
Morishita, T., & Stiavelli, M. 2023, ApJL, 946, L35
Morishita, T., Trenti, M., Stiavelli, M., et al. 2018, ApJ, 867, 150
Nagao, T., Murayama, T., & Taniguchi, Y. 2001, ApJ, 549, 155
Naidu, R. P., Oesch, P. A., Setton, D. J., et al. 2022a, arXiv:2208.02794
Naidu, R. P., Oesch, P. A., van Dokkum, P., et al. 2022b, ApJL, 940, L14
Nicholls, D. C., Kewley, L. J., & Sutherland, R. S. 2020, PASP, 132, 033001
Noboriguchi, A., Inoue, A. K., Nagao, T., Toba, Y., & Misawa, T. 2023, ApJL, 959, L14
Oesch, P. A., Bouwens, R. J., Illingworth, G. D., Labbé, I., & Stefanon, M. 2018, ApJ, 855, 105
Oesch, P. A., Brammer, G., van Dokkum, P. G., et al. 2016, ApJ, 819, 129
Oesch, P. A., Brammer, G., Naidu, R. P., et al. 2023, MNRAS, 525, 2864
Oke, J. B., & Gunn, J. E. 1983, ApJ, 266, 713
Ono, Y., Ouchi, M., Harikane, Y., et al. 2018, PASJ, 70, S10
Osterbrock, D. E. 1978, PNAS, 75, 540
Pacucci, F., Dayal, P., Harikane, Y., Inoue, A. K., & Loeb, A. 2022, MNRAS, 514, L6
Pérez-González, P. G., Costantin, L., Langeroodi, D., et al. 2023, ApJL, 951, L1
Pontoppidan, K., Blome, C., Braun, H., et al. 2022, ApJL, 936, L14
Price, S. H., Bezanson, R., Labbe, I., et al. 2024, arXiv:2408.03920
Richards, G. T., Lacy, M., Storrie-Lombardi, L. J., et al. 2006, ApJS, 166, 470
Rieke, M. J., Baum, S. A., Beichman, C. A., et al. 2003, Proc. SPIE, 4850, 478
Rieke, M. J., Kelly, D., & Horner, S. 2005, Proc. SPIE, 5904, 1
Rieke, M. J., Kelly, D. M., Misselt, K., et al. 2023, PASP, 135, 028001
Roberts-Borsani, G., Treu, T., Chen, W., et al. 2023, Natur, 618, 480
Robertson, B. E., Tacchella, S., Johnson, B. D., et al. 2023, NatAs, 7, 611
Sanders, R. L., Shapley, A. E., Topping, M. W., Reddy, N. A., & Brammer, G. B. 2023, ApJ, 955, 54
Simmonds, C., Tacchella, S., Maseda, M., et al. 2023, MNRAS, 523, 5468
Sobral, D., Matthee, J., Darvish, B., et al. 2018, MNRAS, 477, 2817
Stefanon, M., Labbé, I., Bouwens, R. J., et al. 2019, ApJ, 883, 99
Sun, G., Faucher-Giguère, C.-A., Hayward, C. C., et al. 2023, ApJ, 955, L35
Tang, M., Stark, D. P., Chen, Z., et al. 2023, MNRAS, 526, 1657
Totani, T., Kawai, N., Kosugi, G., et al. 2006, PASJ, 58, 485
Trapp, A. C., & Furlanetto, S. R. 2020, MNRAS, 499, 2401
Treu, T., Roberts-Borsani, G., Bradac, M., et al. 2022, ApJ, 935, 110
Umeda, H., Ouchi, M., Nakajima, K., et al. 2024, ApJ, 971, 124
Verhamme, A., Schaerer, D., & Maselli, A. 2006, A&A, 460, 397
Vijayan, A. P., Lovell, C. C., Wilkins, S. M., et al. 2021, MNRAS, 501, 3289
Wang, B., Fujimoto, S., Labbé, I., et al. 2023a, ApJL, 957, L34
Wang, B., Leja, J., Bezanson, R., et al. 2023b, ApJL, 944, L58
Wang, B., Leja, J., Labbé, I., et al. 2024, ApJS, 270, 12
Weaver, J. R., Cutler, S. E., Pan, R., et al. 2024, ApJS, 270, 7
Wilkins, S. M., Feng, Y., Di Matteo, T., et al. 2017, MNRAS, 469, 2517
Wilkins, S. M., Vijayan, A. P., Lovell, C. C., et al. 2022, MNRAS, 517, 3227
Wilkins, S. M., Vijayan, A. P., Lovell, C. C., et al. 2023, MNRAS, 519, 3118
Williams, C. C., Tacchella, S., Maseda, M. V., et al. 2023, ApJS, 268, 64
Williams, H., Kelly, P. L., Chen, W., et al. 2023, Sci, 380, 416
Yan, H., Ma, Z., Ling, C., et al. 2023, ApJL, 942, L9
Yung, L. Y. A., Somerville, R. S., Finkelstein, S. L., Popping, G., & Dave, R. 2019, MNRAS, 483, 2983
Yung, L. Y. A., Somerville, R. S., Finkelstein, S. L., et al. 2020, MNRAS, 496, 4574
Zavala, J. A., Buat, V., Casey, C. M., et al. 2023, ApJL, 943, L9
Zitrin, A., Zheng, W., Broadhurst, T., et al. 2014, ApJL, 793, L12